Omphacitite formation and fluid-rock interaction processes in an intra-slab eclogite-facies shear zone

Clothilde Minnaert, Samuel Angiboust, Aitor Cambeses, Johannes Glodny, Jesús Muñoz-Montecinos, Antonio Garcia-Casco

LITHOS 484–485 (2024) 107738

Contents lists available at ScienceDirect

LITHOS

journal homepage: www.elsevier.com/locate/lithos

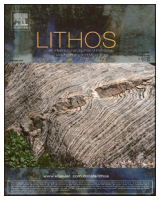

Omphacitite formation and fluid-rock interaction processes in an intra-slab eclogite-facies shear zone

Clothilde Minnaert [a,*], Samuel Angiboust [a,b], Aitor Cambeses [c], Johannes Glodny [d], Jesús Muñoz-Montecinos [e], Antonio Garcia-Casco [c]

[a] ENS de Lyon, University of Lyon, CNRS, LGL-TPE, 46 Allée d'Italie, F-69007 Lyon, France
[b] IUF, Institut Universitaire de France, Paris
[c] Department of Mineralogy and Petrology, Faculty of Sciences, University of Granada, Campus Fuentenueva s/n, 18002 Granada, Spain
[d] GFZ German Research Centre for Geosciences, Telegrafenberg, D-14473 Potsdam, Germany
[e] Structural Geology and Tectonics Group, Department of Earth Sciences, Geological Institute, ETH Zürich, Zürich, Switzerland

ARTICLE INFO

Keywords:
Metasomatism
Fluids
Subduction
Jadeitite
Dissolution-precipitation
Monviso

ABSTRACT

We document the formation of omphacitites in the Monviso Lago Superiore Unit (W. Alps) where eclogite-facies, serpentinite-bearing shear zones host ample evidence for intense intra-slab fluid flow. In the first locality studied, a serpentinite-hosted jadeitite block is rimmed by strained omphacitite (with lawsonite pseudomorphs and minor phengite). U-Th-Pb zircon dating yields a protolith age of c.150 Ma, thus pointing to a burial-related replacement of a former Tethyan seafloor material, and revealed a lack of alpine rims. Multi-mineral Rb-Sr dating of the minerals forming this omphacitite rind yields an isochron age of 41.6 ± 0.7 Ma, corresponding to the early exhumation path still within the eclogite-facies. In this case, omphacitization led to the nearly complete replacement of the former prograde jadeitite through solution-precipitation and was followed by crystal-plastic deformation processes.

In various Monviso localities, Fe-Ti metagabbro blocks (commonly exhibiting brecciated garnetite fragments) display evidence for intense fluid-rock interactions leading to the formation of decimeter-thick, weakly strained omphacite-dominated rinds (with minor amounts of lawsonite, clinochlore and talc) around the blocks at the contact with the surrounding serpentinite. Partly dissolved zircon crystals separated from omphacitite rimming an eclogitic Fe-Ti metagabbro block only yielded middle-Jurassic protolith ages. This indicates that omphacitite rinds did not overgrow the eclogite blocks but rather replaced metasomatically the garnet-rich eclogitic assemblage. The omphacitization overprint occurred independently of the nature of the protolith (namely, forming after a jadeitite or after an Fe-Ti eclogite) as a consequence of infiltration of externally-derived fluids and subsequent element sequestration from the incoming fluid phase. These observations highlight the extraordinary ability of eclogite-facies metasomatic fluids to nearly totally overprint rocks as resistant and impermeable as Monviso eclogite breccias or jadeitites.

1. Introduction

Fluid-rock interaction processes in subduction zones are of major importance for element budgets and recycling as well as for rheological and geodynamic evolution. Metamorphic fluids are released through devolatilization reactions from all subducted lithologies, including sediments, mafic rocks and serpentinites (Peacock, 1990). The fluid source and the amount of fluid released depends on the thermal structure, on the lithological composition of the subduction zone as well as on the initial level of hydration (Van Keken et al., 2011). One of the main fluid-producing reactions in deep subduction systems is the breakdown of serpentinite (variety antigorite; *e.g.* Scambelluri et al., 2004; Padrón-Navarta et al., 2010). It is known to provide a massive amount of aqueous fluids that profoundly impacts the subduction 'factory' in the 80–150 km depth range (*e.g.* Reynard, 2013), thus making this deep subduction environment critical for understanding the plate interface.

Along with geophysical studies, a reliable method to shed light on fluid-rock interaction processes in this depth range is to study exhumed

* Corresponding author.
E-mail address: clothilde.minnaert@ens-lyon.fr (C. Minnaert).

https://doi.org/10.1016/j.lithos.2024.107738
Received 6 February 2024; Received in revised form 19 July 2024; Accepted 22 July 2024
Available online 30 July 2024

portions of former subducted slabs which provide a direct insight into a great diversity of deep subduction environments (*e.g.* Bebout and Penniston-Dorland, 2016; Rubatto et al., 2023). This approach has led to a general view of subduction zones in which some fluids are transferred into the mantle wedge while others travel either along the plate interface itself or along intraslab pathways, channelizing along high permeability zones (*e.g.* Angiboust et al., 2014; Muñoz-Montecinos et al., 2021; Taetz et al., 2018). Fluids can thus travel long distances and be at strong chemical disequilibrium with the rocks they permeate, triggering metasomatic processes. The relative contribution of each fluid source, the pathways and their evolution during subduction history remain unclear. Deciphering changes in the composition of metasomatizing fluids is crucial as it yields information on the fluid source and on the potential fluid pathways from the dehydrating source to the metasomatized rock.

A large variety of rock types are known to derive from fluid-rock interaction under high-pressure/low-temperature conditions (HP-LT), including 'hybrid' schists (chlorite-tremolite and talc schists), lawsonitites, jadeitites and omphacitites (Miller et al., 2009; Tsujimori and Harlow, 2012; Vitale Brovarone et al., 2014). These last two rock types have caught the attention of many researchers for their peculiar mineralogy (*e.g.* García-Casco et al., 2009; Harlow et al., 2015; Shigeno et al., 2012). Two petrogenetic models have been proposed for jadeitite formation: metasomatic replacement of former protoliths (R-type) or direct precipitation from aqueous fluids (P-type; Tsujimori and Harlow, 2012). In a previous petrographic and geochemical study on Japanese rocks, Shigeno et al. (2012) proposed that the two different omphacitite formation processes can occur in the same subduction mélange context. Indeed, determining whether jadeitites and omphacitite formed *via* precipitation or replacement can be challenging, leading to discussions and controversies in the literature (*e.g.* Flores et al., 2013; Hertwig et al., 2016; Yui et al., 2010).

Yet, assessing the origin of jadeitite or omphacitite bodies is crucial to unveal fluid mobility and pathways: while metasomatic replacement involves intense dissolution by a corrosive fluid percolating pervasively the protolith, direct precipitation of jadeitite or omphacitite within veins would suggest that open veins or fractures represent a major fluid pathway. Further investigations on omphacitites are thus needed to understand the various stages of omphacitization as well as the physico-chemical processes at the origin of this phenomenon. Using varied petro-geochemical and geochronological tools, we herein highlight the nature of replacement processes in metasomatized rocks from the Monviso meta-ophiolite and focus on the intensity and nature of channelization of fluid flow at *ca.* 80 km depth in the subduction environment.

2. Geological setting

The Monviso meta-ophiolitic massif, located in the Western Alps (Italy), constitutes an exhumed, 20-km long, continuous section of Tethyan slow-spreading ocean seafloor that was subducted during the Alpine orogeny. It is divided in two main sub- units: the Monviso unit (incipient lawsonite-eclogite facies, to the W) and the Lago Superiore unit, on which we focus (lawsonite-eclogite facies, to the E; Fig. 1a; Lombardo et al., 1978; Angiboust et al., 2012). The Lago Superiore unit is composed of a nearly coherent ophiolitic sequence comprising from the top to the base (i) a sequence of metabasalts and metasedimentary

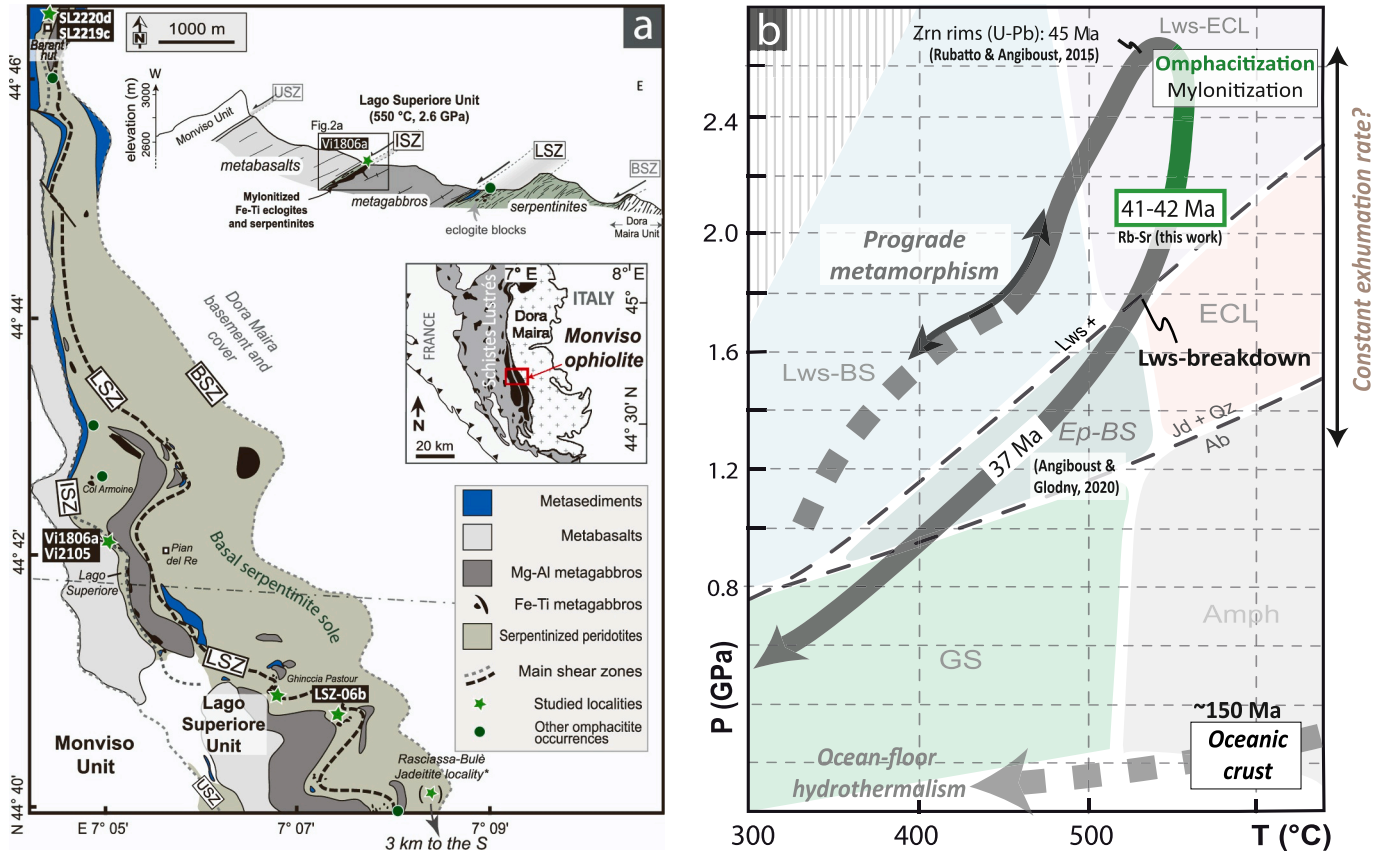

Fig. 1. (a) Simplified geological map of the study area in the Monviso massif localizing the studied omphacitite bodies (green stars) together with previously reported jadeitite/omphacitite localities in the Rasciassa-Bulè region. Also shown is a cross section (modified after Rubatto and Angiboust, 2015) displaying the three main shear zones that cross-cut the Monviso meta-ophiolite (USZ: upper shear zone; ISZ: intermediate shear zone; LSZ: lower shear zone). Inset: regional map localizing the Monviso massif in the Western Alps. (b) Pressure-Temperature path showing the trajectory of the Monviso LSU rocks and the main metamorphic facies (modified after Rubatto and Angiboust, 2015). (For interpretation of the references to colour in this figure legend, the reader is referred to the web version of this article.)

rocks affected by retrogression and shearing, (ii) a variably thick metagabbroic sequence (mainly Mg-Al-metagabbro) and (iii) a "basal" serpentinite sole, several hundred meters thick, (Angiboust et al., 2011) was formed by hydration of a variably depleted harzburgitic protolith (Gilio et al., 2020). Field investigations and petrological studies revealed that the Lago Superiore unit was subducted down to ~80 km depth and subjected to peak metamorphic conditions of 550 °C and 2.7 GPa at 45 Ma (Fig. 1b, Rubatto and Hermann, 2003; Groppo and Castelli, 2010; Rubatto and Angiboust, 2015). The Lago Superiore Unit is crosscut by two major, km-scale eclogite-facies shear zones, respectively localized at the boundary between metabasalts and metagabbros (ISZ: intermediate shear zone) and between metagabbros and the underlying serpentinites (LSZ: lower shear zone; Fig. 1; Philippot and van Roermund, 1992; Angiboust et al., 2011). The top of the thick Mg-Al metagabbro body is capped by a 20–30 m thick layer of fine-grained, mylonitic Fe-Ti metagabbros forming the base of the ISZ and hosting eclogite-facies crack-seal veins, which yielded U-Pb zircon ages of 45 ± 1 Ma (Rubatto and Hermann, 2003). Identical mylonitized Fe-Ti metagabbros fragments are also found in the LSZ, embedded as centimeter-sized to pluri-meter sized, rounded blocks wrapped by talcschists, chlorite schists and serpentinites (Angiboust et al., 2014; Compagnoni et al., 2012). Many of these blocks were brecciated and crosscut by metamorphic veins at high pressure conditions, showing an evolving mineralogical composition in the matrix and veins with highly variable amounts of omphacite, garnet and lawsonite (Locatelli et al., 2018). Most of the Fe-Ti eclogite blocks also exhibit a strongly heterogeneous metasomatic overprint as testified by the formation of lawsonite, phengite, talc-bearing eclogites and chloritites (*e.g.* Angiboust et al., 2014; Gilio et al., 2020; Rubatto and Angiboust, 2015; Spandler et al., 2011). This pervasive fluid flux, of mixed serpentinite-sedimentary signature, is inferred to have occurred in a pulse-like manner (Angiboust et al., 2014; Hoover et al., 2022) under HP-LT peak burial conditions and during early exhumation (Gilio et al., 2020; Locatelli et al., 2019) as a consequence of antigorite and brucite dehydration (*e.g.* Schwartz et al., 2013).

Along with typical eclogites, jadeitites and omphacitites (rocks containing >80 vol% of omphacite) are two emblematic lithologies of the Monviso massif which have been extensively quarried during Neolithic times (*e.g.* Pétrequin et al., 2011). Even though jadeitite has been suspected in the Monviso meta-ophiolite already more than a century ago (Franchi, 1900), the first report of a potential source area in the Punta Rasciassa region has been described only in the 2000's (Compagnoni and Rolfo, 2003). There, jadeitite blocks associated with the basal serpentinites have been interpreted as former metaplagiogranites variably transformed into quartz-bearing jadeitites during alpine metamorphism (Compagnoni et al., 2007; Compagnoni et al., 2012). A jadeite-bearing metaplagiogranite described further south along the LSZ in the Verné region by Castelli et al. (2002) supports this hypothesis and yielded a 152 +/− 2 Ma U-Pb age, interpreted as the zircon crystallization age during the magmatic activity associated with the opening of the Tethyan basin (Lombardo et al., 2002). It is likely that most of the jadeitite blocks were displaced during Quaternary mass-slide processes, and thus the pristine block-in-matrix structure remains to be documented. Lawsonite-bearing omphacitite blocks are reported by Compagnoni et al., (2012) close to the Punta Rasciassa area but no petrological data are available. Another omphacitite occurrence is described by Castelli and Lombardo (2007) as dm-thick boudins at the contact between the Verné metaplagiogranite and the basal serpentinite. They infer from the composition in major and trace elements that this omphacitite was formed by the metasomatic replacement of a gabbronorite during interactions with the surrounding ultramafic rocks.

3. Analytical methods

Further details on analytical techniques are provided in the supplementary materials. All the mineral abbreviations are after Whitney and Evans (2010).

Scanning Electron Microscopy (SEM) was carried out using a Zeiss Evo MA10 and a Zeiss Supra 55 VP machine at the Institut de Physique du Globe de Paris and ENS Lyon respectively, operated at an acceleration voltage of 15 kV using internal calibration standards. Electron probe microanalyses (EPMA) were performed at the Centre for Scientific Instrumentation of the University of Granada (CIC-UGR) and at the CAMPARIS analytical facility in Sorbonne University. Cathodoluminescence images were acquired with a Cathodyne (NEWTEC) machine at IPGP coupled to an optical microscope operated at 13 kV and 120 μA plasma with an exposure time of 2 s per image.

Representative samples of jadeitite and omphacitites were crushed and pulverized to determine major and trace element concentrations through X-ray fluorescence (XRF) and inductively coupled plasma mass spectroscopy (ICP-MS) at the CIC-UGR. Zircon crystals were analyzed at the CIC-UGR with the IBERSIMS SHRIMP IIe/mc ion microprobe.

For Rb-Sr mineral dating, one small (200 g) phengite-rich omphacitite sample was crushed for mineral separation. Rb-Sr isotopic data were obtained at GFZ Potsdam on a Thermo Scientific TRITON thermal-ionization mass spectrometer. Uncertainties of isotope and age data are quoted at 2σ throughout this work.

4. Field relationships

Clinopyroxenites (jadeitites and omphacitites) had been reported so far in two areas of the Monviso massif serpentinites, both located in the southern portion of the Lago Superiore Unit (*e.g.* Castelli and Lombardo, 2007; Compagnoni et al., 2007). Our field observations have been carried out on the central and northern portion of the massif, where we observed *in situ* omphacitite-bearing block rims in various localities including the Barant region, Ghinccia Pastour hill, Colle Armoine and Punta Murel areas. We herein mainly focus on two key localities (Fig. 1a): the Pian del Re/Rocce Alte area (omphacitite forming around jadeitite) and the Punta Barant area (omphacitite forming around Fe-Ti eclogite). The Ghinccia Pastour and Punta Forcione localities also exhibit important macroscopic and microscopic features that will be presented below.

4.1. Rocce Alte omphacitite-jadeitite block

The studied exposure is located in the NE cliff of Rocce Alte mtn. at c.2400 m elevation, above the Po spring near Pian del Re locality (Fig. 1a). There, a several tens of meters-thick shear zone (the "intermediate shear zone", ISZ) separates the overlying metabasalts sequence to the SW from a 200 m-thick sheared metagabbro sliver to the NE (Fig. 2a). The shear zone contains decameter-sized lenses of calcschists, metabasalts, eclogites and a few meter-sized clinopyroxenite blocks (jadeitites - omphacitites), all wrapped within antigorite-schists associated with minor talcschists and tremolitite along the lens-matrix boundaries (Fig. 2b). Talc and chlorite-rich lithologies, poorly exposed in the studied outcrop, exhibit elongated flakes with their long axes parallel to the block edge (Fig. 2b). Similar blackwalls were reported by Compagnoni et al. (2012) and Angiboust et al. (2014) for mafic blocks from the Lower Shear Zone (LSZ; Fig. 1a) in southern Monviso massif. The outer block is made of a strained, deep-green foliated omphacitite with up to mm-sized large phengite laths underlining the foliation. Pseudomorphs after lawsonite form either whitish quadrangular patches or continuous, mm-thick whitish bands that follow the main rock foliation. Towards the core of the pod, the strain and the amount of omphacite decrease while the amount of jadeite increases (Fig. 2c). For this study, we selected one jadeitite sample from the block core (Vi1806a; Fig. 2d) and one omphacitite sample from the block rim (Vi2105; Fig. 2e).

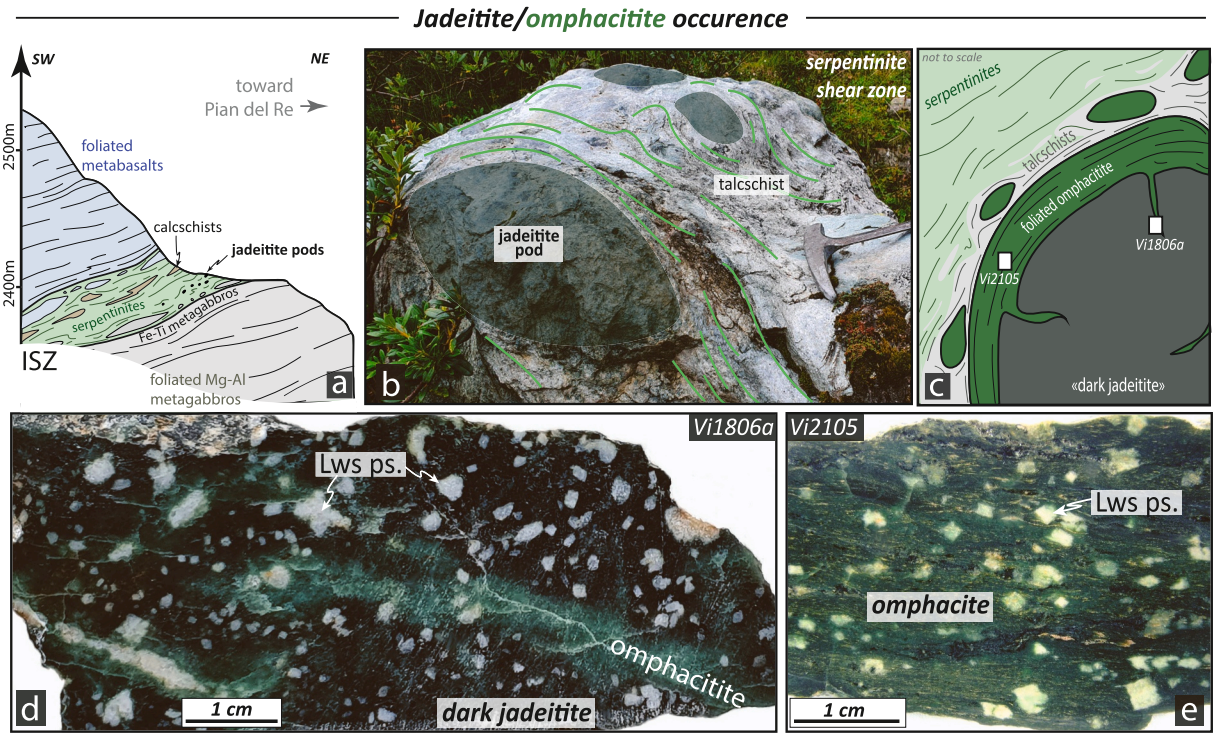

Fig. 2. (a) Simplified cross section showing the structural setting in the new jadeitite-omphacitite locality of Rocce Alte. (b) Field picture showing one of the (rare) blocks embedded in the host ISZ serpentinite. (c) Sketch highlighting structural relationships between the block core, the rim and the host. (d) Hand specimen picture of the dark jadeitite (block core) exhibiting numerous lawsonite pseudomorphs in the matrix as well as the late formation of omphacitite. (e) Hand specimen picture of the omphacitite showing the mylonitization and the lawsonite porphyroblasts that overgrow the deformed matrix.

4.2. Omphacitite-bearing Fe-Ti eclogite (Barant, Ghinccia Pastour, Punta Forcione)

The main eclogite/omphacitite outcrop considered in this study is located in the northernmost part of the ophiolitic massif in the SW face of Punta Barant. There, the structural relationships between the different lithologies differ from the central part of the massif (Figs.1a, 3a, see also Balestro et al., 2011). No clear distinction can be made between the ISZ and the LSZ shear zones as the mafic portion of the former oceanic crust is particularly discontinuous in this area. A metasedimentary sequence (hundreds of meters thick) comprising calcschists with marble layers overlies the sheared basal serpentinite; the latter hosting Fe-Ti eclogite blocks. Upwards, the metasediments are crosscut by an anastomosed shear zone, tens to hundreds of meters thick, and characterized by mylonitic serpentinite embedding numerous blocks (pluri-meters sized) displaying typical features of Monviso Fe-Ti eclogites in their core (breccia made of mylonitized eclogite clasts cemented by a garnet- and omphacite- bearing matrix; see Angiboust et al., 2012 and Locatelli et al., 2019 for further details). The blocks are wrapped by talcschists and chlorite schists forming a blackwall and containing rare carbonates, whereas the interblock matrix of the shear zone is formed by antigorite schists. In most of the blocks, garnet-rich lithologies, breccias and garnetite fragments forming the block core are sharply replaced by a garnet-free, omphacite-dominated matrix surrounding the block (hereafter referred to as omphacitite; Fig. 3). These cortices are of variable thickness, ranging from a few centimetres up to 50 cm, and range from an almost pure omphacitite composition to a lawsonite-rich (up to 25% vol.) lithology (**Fig.S1d**). The omphacitized block rims are generally poor in rutile although thin (mm to cm-thick) bands enriched in this mineral are locally visible, often associated with chlorite and postdating the omphacitite matrix. The outermost part of the omphacitite is variably sheared and exhibits local brecciation and cementation by clinochlore and rutile crystals (Fig. 3h). Lawsonite pseudomorphs are found embedded within clinochlore and texturally associated with omphacite and rutile or ilmenite (**Fig.S1b**). Chalcopyrite is also found in a few omphacitite cortices, growing in apparent textural equilibrium with omphacite (**Fig.S1c**) and occasionally associated with late glaucophane. In retrogressed marginal domains, blue amphibole clearly post-dates the omphacitite matrix, and is locally associated with dolomite, clinozoisite and chlorite in late crosscutting veins (see **Fig.S1a**)

In Ghinccia Pastour and Punta Forcione localities (central Monviso massif; Fig. 1a) omphacitized eclogite breccias blocks are also found embedded in serpentine schists of the LSZ (see Angiboust et al., 2011; Angiboust et al., 2014; Locatelli et al., 2018 and section 5.3 for more details).

5. Petrography, mineral chemistry and microstructures

5.1. Rocce Alte jadeitite/omphacitite

5.1.1. Jadeitite description

Among the different jadeitite samples collected, sample Vi1806a represents the most pristine and less affected by albitization during exhumation. In the dark regions of this sample, the rock is made of hundred-µm large jadeite crystals (Fig. 4a, XJd = 0.88–0.98, see **Table A1** for composition analysis). The sample also hosts euhedral sub-millimeter to millimeter-sized phengite (Si = 3.60–3.75 atoms per formula unit; apfu) and lawsonite laths (Fig. 4d,e), the latter replaced by clinozoisite (locally epidote, X_{Fe3+} = 0.01–0.23), paragonite and albite (Fig. 4d,e,f). Sample Vi1806 exhibits variable degrees of omphacitization along grain boundaries and along cracks (Fig. 2d, Fig. 4b, Fig. 5b,c). Omphacite has almost continuous compositions along the jadeite exchange vector, ranging from XJd = 0.78 to XJd = 0.49 (classification after Morimoto, 1989). Textural observations show micrometer-sized inclusions of omphacite (Fig. 4c) in dark jadeite crystals, evidencing that the original jadeite is replaced by omphacite *via* transient porosity creation and dissolution-precipitation processes (Putnis, 2015). Cathodoluminescence imaging reveals jadeite-rich cores (colored in

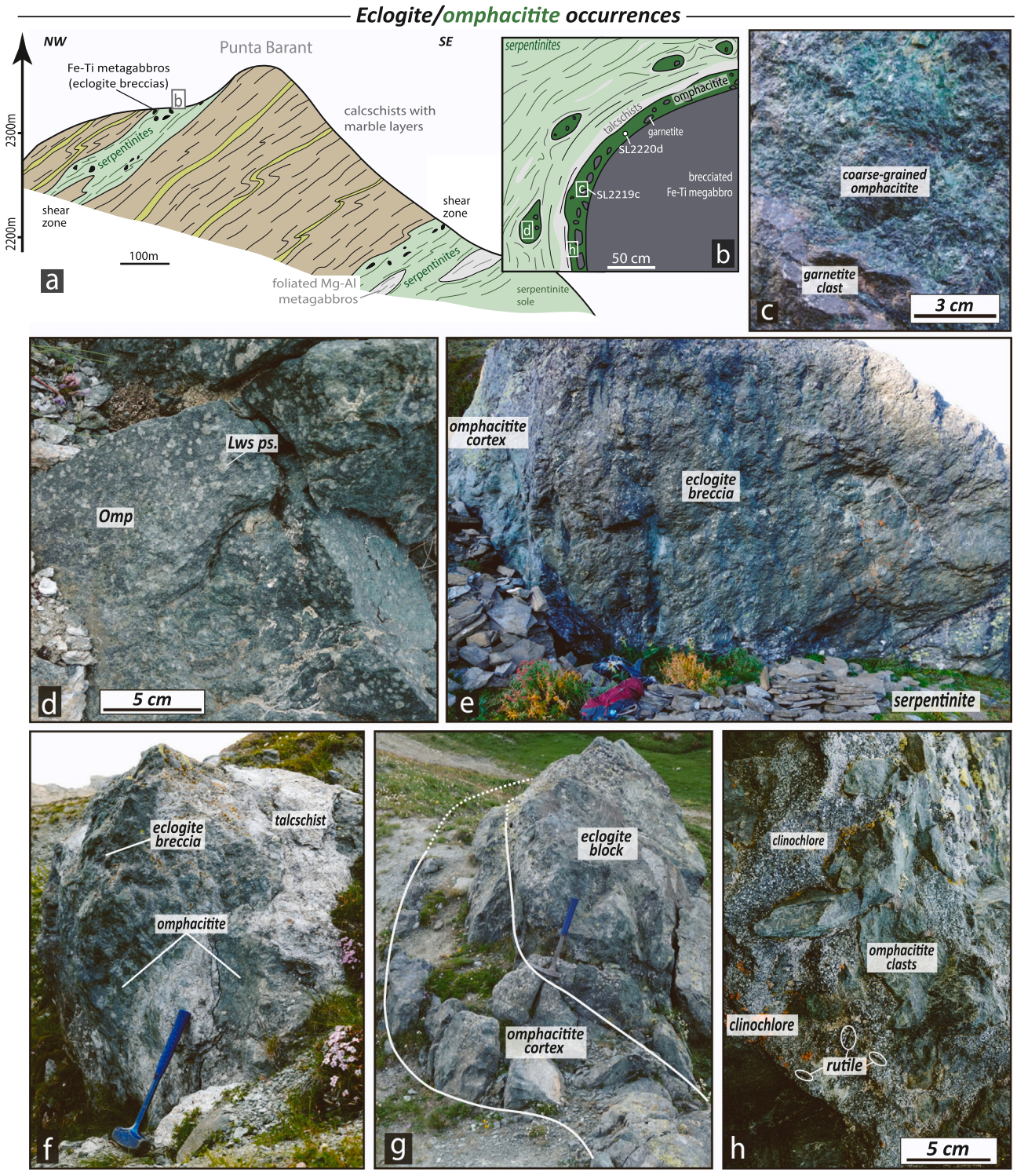

Fig. 3. (a) Simplified cross section showing the structural setting at the eclogite-omphacitite locality of Barant. (b) Sketch highlighting the structural relationships between the block core, the rim and the host. (c) Field picture showing a garnetite fragment surrounded by a coarse-grained omphacitite (d) Picture of a lawsonite-bearing omphacitite. (e), (f) and (g) Field pictures of the Fe-Ti eclogite blocks showing their omphacitite cortex and their relationships with the host ultramafics. (h) Picture of omphacitite clasts from an outer block rim sealed by a clinochlore-rich matrix.

yellow-green on Fig. 4g), brown jadeite-omphacite rims and omphacite in light purple. Along the margins of the vein domain, the jadeite-rich cores were dissolved along their rims and replaced by a CL-purple omphacite (Fig. 4g; see also section 9.3). In the matrix, omphacite-bearing cracks are observed connecting phengite and lawsonite pseudomorphs (Fig. 4e,g; **Fig.S2b**). The whitish cracks visible on the hand specimen (Fig. 2d) correspond to CL-purple to blueish domains, mostly composed of clinozoisite intergrown with a CL-paler omphacite (Fig. 4g). Texturally late albite (associated with chlorite) is common in the vicinity of lawsonite pseudomorphs, along cracks and grain boundaries (Fig. 4e). Bright zircon crystals (in CL and BSE imaging modes) are ubiquitous in sample Vi1806a (Fig. 4a, **Fig.S2a**). Rutile has also been observed in the matrix and in the mineral separate. Details on mineral chemistry are provided in **Fig.S3b**.

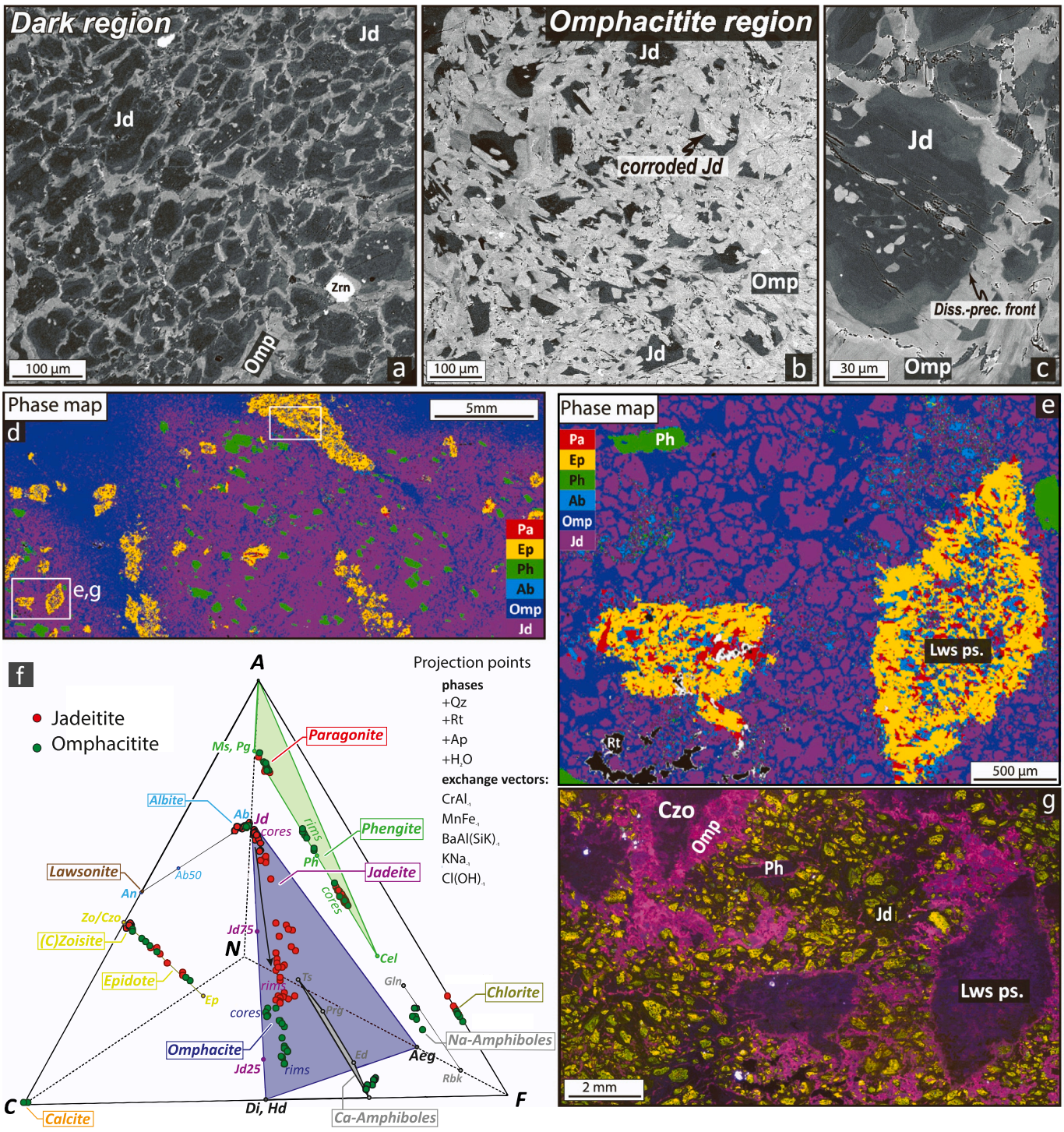

Fig. 4. Pictures and chemical characterization of the jadeitite sample Vi1806a (Rocce Alte). (a) BSE (backscattered electron) picture of the dark jadeitite highlighting enrichments in omphacitic component of clinopyroxenes along grain boundaries. Note the absence of apparent strain in the matrix. (b) BSE image showing an area that has undergone extensive transformation into omphacitite. (c) Close up view on a jadeitite crystal that exhibits coupled dissolution-precipitation replacement of jadeitite into omphacite along rims (note the apparent porosity creation associated with the replacement process; see also Putnis, 2015). (d) EPMA-based phase map highlighting the omphacitization front in the jadeitite. White rectangles indicate close-up views shown in (e) and in appendix. (e) Phase map showing a close-up view of lawsonite pseudomorphs. (f) Mineral compositions from jadeitite and omphacitite, in the Na_2O-Al_2O_3-CaO-(FeO + MgO) system, projected from the phases and exchange vectors indicated. (g) Cathodoluminescence image showing lawsonite pseudomorphs and omphacite replacing jadeitite.

5.1.2. Omphacitite description

The sample Vi2105 exhibits a fine-grained omphacite-bearing foliation associated with elongated phengite flakes and lawsonite pseudomorphs, along with numerous stringers of rutile (Fig. 5a,b,c). Phengite exhibits a thin muscovite-rich rim around Si-rich cores (~3.70 apfu). Lawsonite porphyroblasts are now completely replaced by clinozoisite ($X_{Fe3+} = 0.03–0.25$), paragonite and chlorite. They apparently overgrow an already foliated matrix as they contain both omphacite and rutile inclusions with the same orientation as grains in the matrix (Fig. 5b). Omphacite from the matrix is slightly zoned with relatively darker

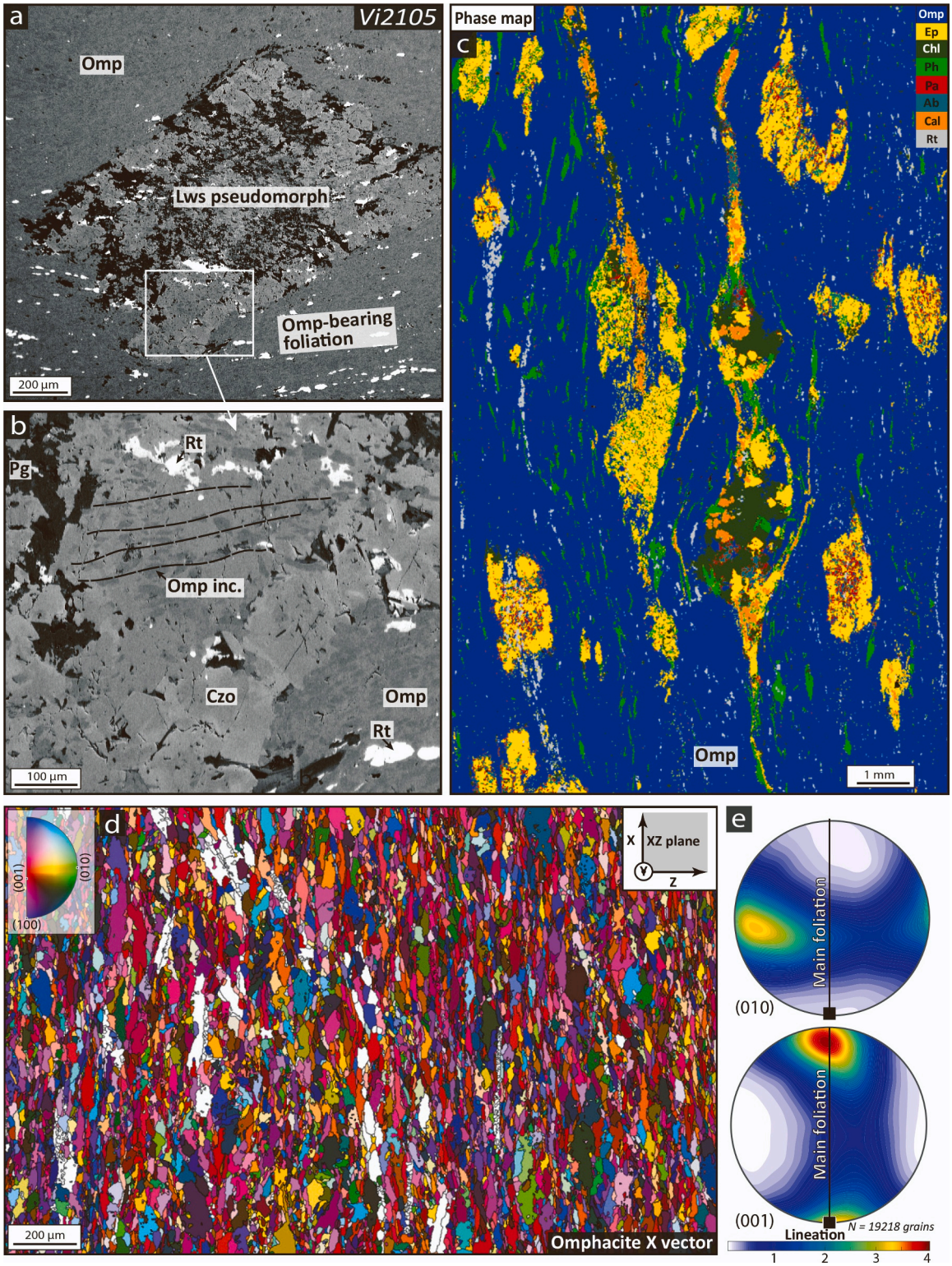

Fig. 5. Mineral and fabric characterization of the omphacitite sample Vi2105 (Rocce Alte) (a) BSE image showing the omphacite-rich matrix that hosts lawsonite pseudomorphs with oriented clinopyroxene inclusions. Bright ribbons correspond to rutile crystals. (b) Close up view of the lawsonite pseudomorphs that host both oriented rutile and omphacite crystals parallelized with the matrix foliation (dotted black lines indicate the intra-lawsonite foliation). (c) EPMA-based phase map showing the foliated omphacitite containing oriented phengite, rutile and variably deformed lawsonite pseudomorphs. A rounded chlorite-rich aggregate in the center of the map may derive from the retrogression of a previous garnet crystal (note that garnets of average composition $Alm_{59}Gr_{19}Py_{19}Sp_{03}$ were found during mineral separation process but not observed in the thin section) (d) Orientation map colored according to the inverse pole figure key (IPF) of omphacite (top left panel). View (XZ plane) corresponding to the X axis of the finite strain ellipsoid shown in the top right panel. (e) Pole figure diagrams represented in an upper hemisphere equal area projection for omphacite (010) and (001), top and bottom, respectively. The data points plotted in the pole figure diagrams correspond to one point per grain. The orientation map displayed in panel (d) has been cropped out for aesthetic purposes.

jadeite-richer cores and brighter omphacite-richer rims (Fig. 5a,b, XJd ranging from 0.22 to 0.49), even displaying locally diopsidic compositions. No near-pure jadeite (as the one forming the crystal cores in the jadeitite sample Vi1806a) was found in this sample. Pyrite is locally very abundant, as sub-millimetric crystals underlining the omphacitite foliation. Calcite and to a minor extent glaucophane are also locally observed in the trails of strained pseudomorphs after lawsonite (Fig. 5c).

The omphacite microfabric is characterized by fine-grained, roughly equigranular grains with grain diameters mostly below 30 μm (see the histogram in **Fig. S4a**) and elongated-tabular crystal shapes. This fabric displays a crystallographic preferred orientation (CPO) characterized by the (001) poles oriented perpendicular to the poles of the foliation and parallel to the lineation orientation (Fig. 5d,e), while the (010) poles display a weaker CPO and a girdle with the maxima oriented parallel to the poles of the foliation, thus defining a fabric comparable to a L-type (in the sense of Zhang et al., 2006). Furthermore, no significant degrees of misorientation are observed, with the exception of a few grains (**Fig. S4a**).

5.2. Barant omphacitized Fe-Ti eclogite

The omphacitite sample SL2219c contains ~80 vol% of omphacite and ~ 20 vol% of garnet forming two pluri-millimeter-thick garnetite bands (see for instance **Fig.S5**). Omphacite is euhedral to subhedral and grains exhibit prismatic habits, range in size from 200 μm to 1 mm and are chemically zoned (Fig. 6a). The grain cores (typically $Di_{53}Jd_{41}Aeg_{07}$, see Fig. 6g and **Table A1** for composition analysis) were partly dissolved and replaced along their rim by a more jadeitic composition (typically $Di_{42}Jd_{48}Aeg_{10}$). Late pyroxene generations occur along grain boundaries, variably enriched in Ca-Mg-Fe^{2+} (XQuad up to 0.8) and aegirine ($Di_{57}Jd_{23}Aeg_{20}$). Texturally late phases are locally found, including chlorite (XMg = 0.79–0.83), epidote (X_{Fe3+}=0.14–0.20), albite and phengite (Si = 3.30–3.37 apfu). Small rutile grains, apatite and large zircons (>500 μm) also occur in this sample, particularly in the garnetite bands. These garnetite bands display a large number of atoll-shaped garnet crystals with omphacite replacing their cores (**Fig.S2f** and **S2g**). Relict garnet grains exhibit irregular shapes and truncated zoning patterns that suggest intense dissolution along their rims. They are also observed within the omphacitite domain in the garnetite vicinity. Most of the garnets have a size below 100 μm but larger relicts (>500 μm) also occur locally (Fig. 6b). The larger grains are moderately zoned, mainly with an increase in the pyrope component at the expense of grossular (from $Alm_{54}Gr_{29}Py_{14}Sp_{03}$ in the core to $Alm_{60}Gr_{15}Py_{23}Sp_{02}$ in the rim, see **Fig. S3a**). The spessartine component shows a general decrease from core to rim with noticeable 100-μm scaled chemical oscillations (Fig. 6c). The garnet inner cores are Cr-poor (Cr_2O_3 ~ 0.01 wt%, Fig. 6b) while the mantle and rims have higher chromium content (up to Cr_2O_3 ~ 1.5 wt%), displaying a strong oscillatory zoning pattern. This zoned garnet was partly dissolved and overgrown by a later, Cr-poor garnet generation partly coinciding with the latest spessartine-rich generation

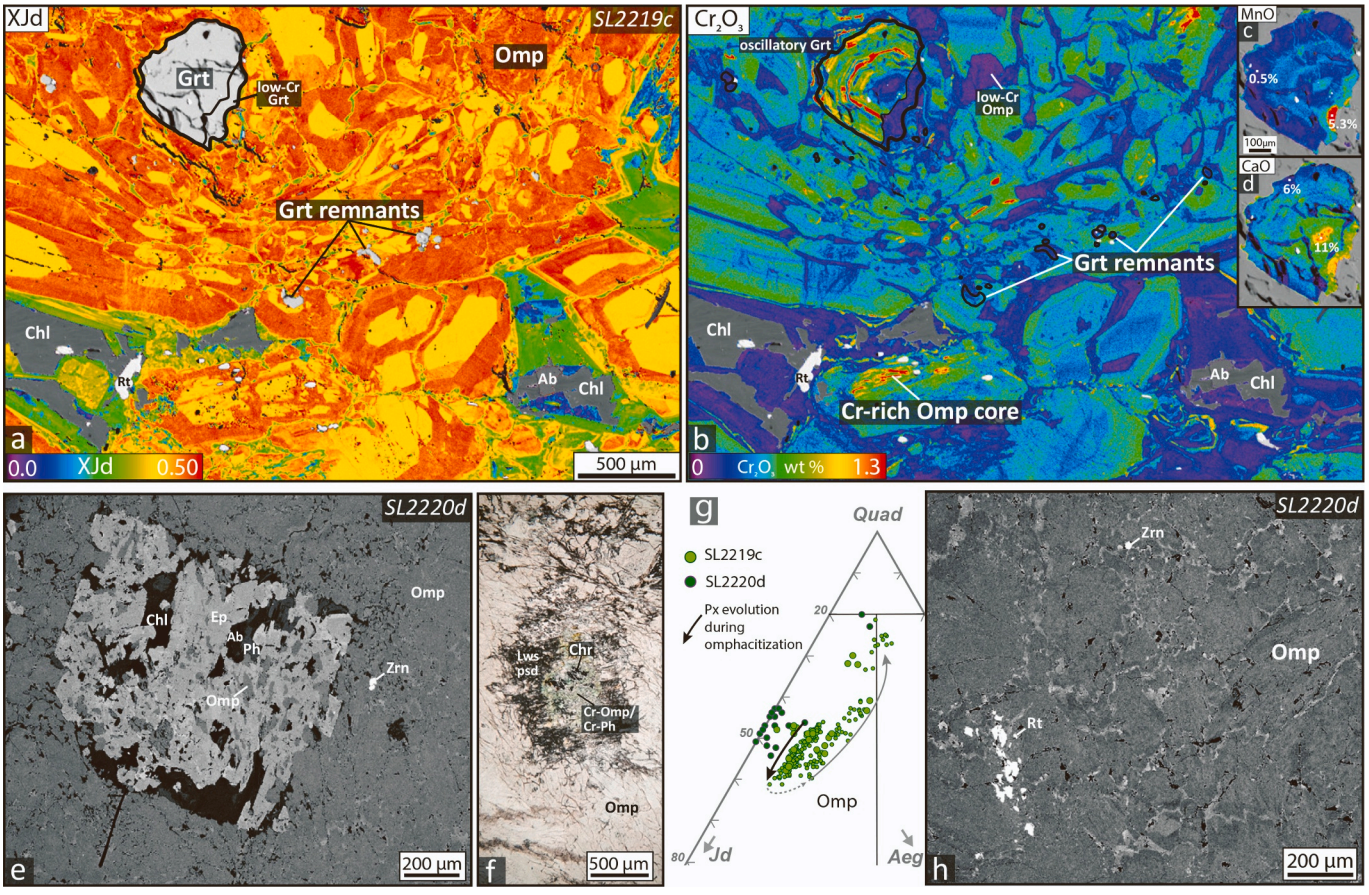

Fig. 6. (a) X-ray map showing the jadeite content in clinopyroxenes (the other phases are masked out) in the Barant omphacitite SL2219c. (b) X-ray map of the same area showing Cr_2O_3 (wt%) in clinopyroxene and garnet. Note the oscillatory zoning in both garnet and omphacite. Some omphacite cores are rich in Cr while the rims are Cr poor. Also note the Cr-poor overgrowth of the large garnet grain. (c) and (d) Close-up view of the large garnet remnant displaying respectively the MnO and CaO (wt%) contents. (e) BSE image of a pseudomorph after lawsonite and the omphacite matrix in the omphacitite sample SL2220d. (f) Optical microscope image of a lawsonite pseudomorph showing chromian spinel relicts in its core, surrounded by Cr-rich omphacite and phengite. (g) Ternary diagram of clinopyroxene compositions (after Morimoto, 1989) in Barant omphacitite. (h) BSE image of the omphacite matrix containing rutile and zircon. Omphacite grains show a slight chemical zoning with darker rims and a bright, more diopsidic, late generation along grain boundaries.

($Alm_{45}Gr_{18-29}Py_{14-21}Sp_{10-13}$, Fig. 6c). Oscillations in chromium content also appear in omphacite (Fig. 6b) and some grains have a Cr-enriched core. Moreover, the omphacite containing a high jadeite content displays two clusters of Cr-concentration. The first cluster contains a moderate amount of chromium ($Cr_2O_3 \sim 0.5$ wt%) while the other is Cr-poor ($Cr_2O_3 < 0.05$ wt%). Cathodoluminescence imaging of one of the largest zircon grains displays numerous dissolution features, thin overgrowths and close spatial association with rutile and apatite **(Fig.S2e)**.

The omphacitite sample SL2220d is mainly made of omphacite (~85% vol%) associated with lozenge-shape, mm-sized whitish patches interpreted as lawsonite pseudomorphs (Fig. 6e,f) and locally with a small amount of talc. Omphacite displays subhedral to anhedral shapes (Fig. 6h), is low in aegirine component and shows core to rim zoning towards more jadeitic compositions ($Di_{57}Jd_{42}Aeg_{01}$ to $Di_{49}Jd_{51}Aeg_{00}$, **Fig.S6b**). Omphacite grains also display Cr-enrichment in their core and oscillatory zoning in chromium, in a similar way as in sample SL2219c (**Fig.S6a**). Pseudomorphs after lawsonite have been replaced by epidote ($X_{Fe3+=}$0.09–0.13), phengite (Si ~ 3.35 apfu), albite and clinochlore (Fig. 6f). Locally, Cr-spinels (Cr# ~0.9) are found in the core of lawsonite pseudomorphs and are surrounded by Cr-enriched omphacite (Cr_2O_3 up to 5.0 wt%; Fig. 6f). Omphacite grain boundaries are lined with a brighter clinopyroxene on BSE images due to an enrichment in diopside component (typically $Di_{80}Jd_{13}Aeg_{07}$). Rutile and zircons also occur in omphacite domains.

5.3. Ghinccia Pastour - Punta Forcione omphacitites

Decimeter-sized, reddish garnetite fragments sparsely occur in omphacitized block rims (Fig. 7a). Centimeter-sized, euhedral garnet crystals occur in some regions of the omphacitite while other regions are devoid of garnet grains. A wide diversity of hydrous minerals such as lawsonite, clinochlore or talc can be observed in the omphacitite matrix. These omphacitite rinds are characterized by the formation of Cr-rich omphacite along grain boundaries and by the formation of garnet displaying oscillatory and patchy zoning in chromium **(**Fig. 7b**).**

6. Whole-rock chemistry

Whole-rock composition in major elements is close to an omphacite (or jadeite) composition, in agreement with the clinopyroxene-dominated mineralogy (**Table A2**), although some peculiarities can be noticed. The jadeitite sample (Vi1806a) is substantially richer in TiO_2 (1.15 wt%) and K_2O (0.60 wt%) than Monviso jadeitites analyzed by Compagnoni et al. (2012). The omphacitite (sample Vi2105) found as a rim around jadeitite has slightly higher TiO_2 (1.58 wt%) and K_2O (0.89 wt%) content than the jadeitite. This composition reflects the presence of significant amounts of rutile and phengite in both samples. The omphacitite found around a Fe-Ti eclogite block (sample SL2220d) has similar major element concentration to the one surrounding the jadeitite, but is paradoxically characterized by its lower iron content (FeO = 3.26 wt% compared to 5.90 wt% in sample Vi2105) and in titanium (TiO_2 = 0.11 wt%). N-MORB-normalized trace element patterns (Fig. 8) reveal that both the jadeitite core and its omphacitite rim are enriched in LILEs (Large Ion Lithophile Elements). The highest enrichments, up to 2 orders of magnitude, are in Cs, Rb and K, while Sr is close to the N-MORB value in the omphacitite and slightly enriched in the jadeitite. The REEs patterns of both samples are similar, except for a higher content in all REEs in the omphacitite compared to the jadeitite (consistent with a crystal chemistry effect). The patterns show no Eu anomaly, and a general decrease from LREEs to HREEs. LREEs are enriched relative to N-MORB while HREEs are depleted. These patterns strongly contrast with those measured in Monviso jadeitite and quartz-bearing jadeitite by Compagnoni et al. (2012), that show a clear negative Eu anomaly, an enrichment in all other REEs and a flat to slightly increasing pattern. High field strength elements (HFSEs), Th, U, Cr, and Ni show more variability between the jadeitite and the omphacitite. The jadeitite is enriched in Th, U, Hf, Zr (up to one order of magnitude) whereas the omphacitite is poorer in these elements (slightly enriched to slightly depleted). Conversely, the jadeitite is depleted in Cr and Ni while the omphacitite Vi2105 displays a slight enrichment in both elements. The omphacitite SL2220d clearly differs from the two previous samples. This omphacitite sample is moderately enriched to depleted in LILEs (up to one order of magnitude) and lies within the Fe-Ti eclogite field for those elements. The REEs are all depleted relative to N-MORB and the pattern increases gently towards the HREE, associated with a small Eu positive anomaly. HFSEs are either close to N-MORB/Fe-Ti eclogites values (Zr) or fairly depleted. The contents of Ni and more markedly Cr are high relative to both Fe-Ti eclogite and N-MORB (close to 10 times as much chromium as in N-MORB).

7. Geochronology

7.1. Zircon U-Pb geochronology

The jadeitite sample Vi1806a contains abundant, medium sized (150 × 100 μm) zircons. They are transparent and translucent, forming

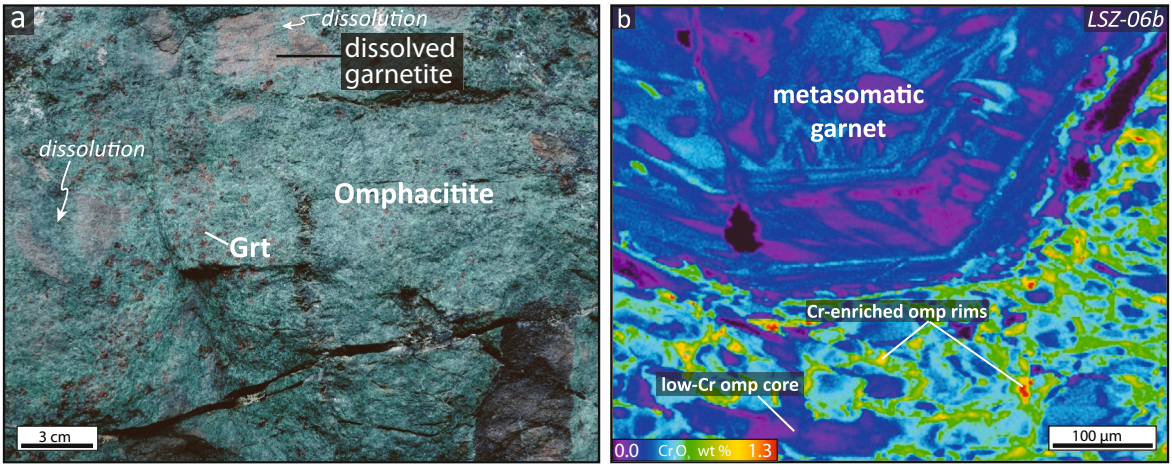

Fig. 7. (a) Field picture of a block cortex near Ghinccia Pastour locality showing partly dissolved garnetite fragments (from the original eclogite breccia) in an omphacitite matrix. Garnetite fragments exhibit irregular morphologies as well as finger-shaped dissolution patterns. (b) X-ray map of the Cr_2O_3 (wt%) content in the metasomatic sample LSZ-06b. Note the oscillatory nature of the garnet zoning pattern and the omphacite matrix around, which is enriched in Cr along grain boundaries.

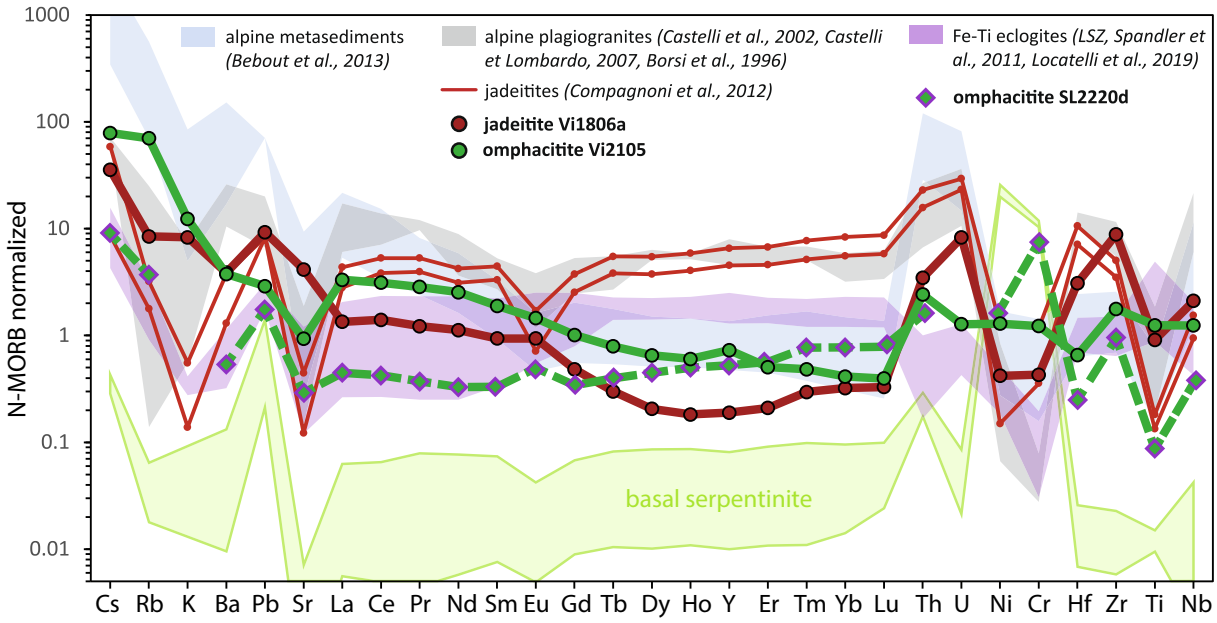

Fig. 8. N-MORB normalized trace element diagram showing the composition of alpine plagiogranites, Monviso jadeitites (from the literature) together with the jadeitite and two omphacitites analyses presented in this study. Monviso serpentinites (from Angiboust et al., 2014) and alpine metasediments (from Bebout et al., 2013) are also shown for comparison.

euhedral to subhedral prismatic bipyramids, although many grains show broken morphologies and contain abundant inclusions and fractures (Fig. 9a). The cathodoluminescence images reveal that zircons are composed of irregularly distributed bright white or grey areas in the outer rims, whereas the inner parts display concentric oscillatory zoning (Fig. 9a). Twenty-two SHRIMP U-Th-Pb measurements on 21 zircon grains yielded low concentrations of U (18–271 $\mu g.g^{-1}$) and Th (7–252 $\mu g.g^{-1}$) with Th/U = 0.24–1.26 and a contribution of common lead (f^{206} = 0–4.33%) (**Table A4**). Some analyses are discordant (discordance = −1.8 to 36%). We applied a ^{204}Pb-based correction that corrected the majority of data to concordia (Fig. 9c). Results of this correction approach are virtually identical to ^{207}Pb-corrected data. The weighted

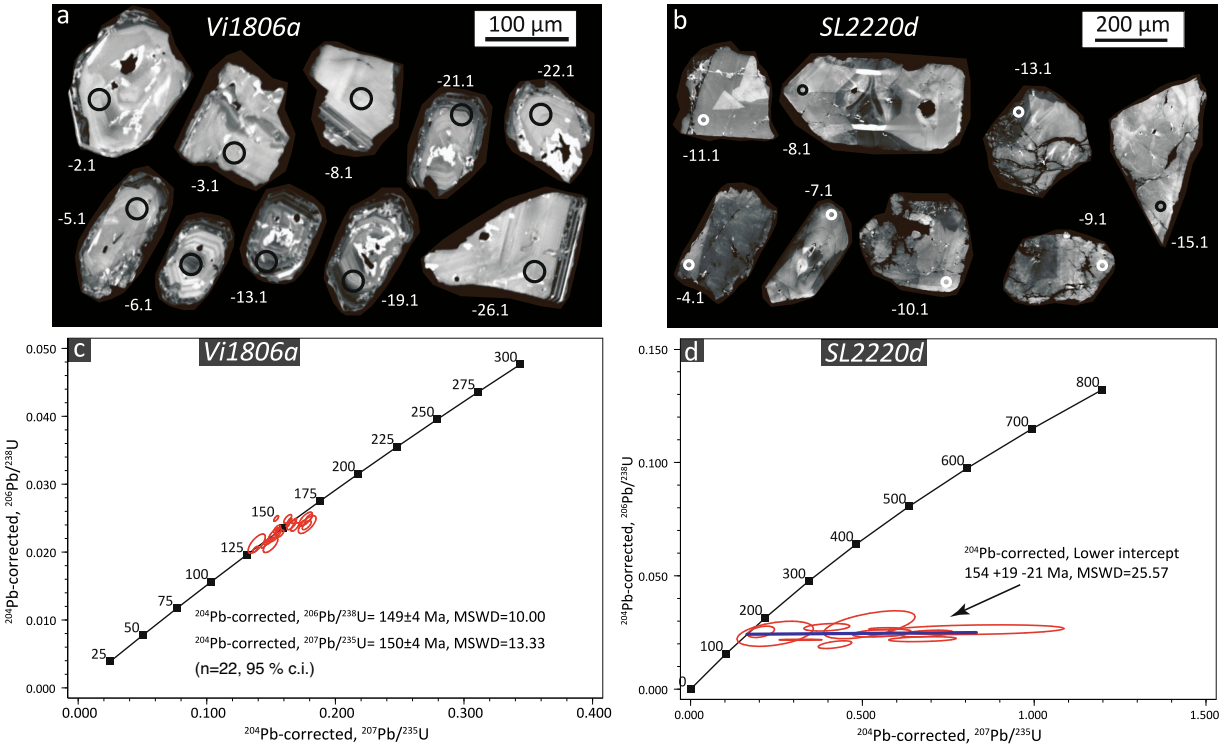

Fig. 9. (a) Cathodoluminescence images of zircons recovered from the jadeitite sample Vi1806a. Note the irregular morphologies and overgrowth at the outer rim of the grains. (b) Cathodoluminescence images of zircons recovered from the sample SL2220d. (c) Wetherill concordia plot (^{204}Pb-based common-lead corrected) of the jadeitite zircons found in sample Vi1806a. (d) Wetherill concordia plot (^{204}Pb-based common-lead corrected) of the 12 discordant zircons found in the sample SL2220d (see Table A4).

means (errors reported at 2σ) of the ^{204}Pb-corrected ^{206}Pb/^{238}U data yield an age of 149 ± 4 Ma (MSWD = 10) (Fig. 9c).

Omphacitite sample SL2220d contains relatively abundant and large (300 × 200 μm) zircon grains (Fig. 9b). They are whitish to translucent, often with pseudo-octagonal sections forming euhedral to subhedral bipyramid prisms. Many grains are broken (likely during the milling process) and transected by fractures (Fig. 9b). Cathodoluminescence images show a sector to concentric oscillatory zonation that alternates high cathodoluminescence and darker bands. Twelve measurements in 12 grains have been performed in zircons from sample SL2220d. They have low U (7–19 μg.g^{-1}) and Th (3–12 μg.g^{-1}) with Th/U = 0.4–0.7. These zircons have very low concentrations of radiogenic ^{206}Pb and ^{207}Pb but somewhat elevated common lead (f^{206} = 0–10.31%). This hinders U-Pb age calculations due to the high discordance (discordance = 45–73%). However, the discordance decreases using 204Pb-based common-lead model and the analyzed spots, which allows to estimate a discordia line intercepting the concordia at 154 + 19–21 Ma (MSWD = 26) **(**Fig. 9d**).**

7.2. Rb-Sr geochronology

Multimineral Rb-Sr dating is a well-established geochronological method for dating the waning stages of dynamic recrystallization of mica in equilibrium with other, simultaneously recrystallizing Sr-bearing phases (Freeman et al., 1998; Inger and Cliff, 1994), provided that no later thermal-diffusive or retrogressive reactive overprint occurred. Temperatures well above 600 °C are required to reset the Rb-Sr-system in mica *via* diffusional processes (Glodny et al., 2008), while crystal- plastic deformation may reset the Rb/Sr system of mica at temperatures as low as 300 °C (Müller et al., 1999). This method has been applied here on the omphacitite sample Vi2105 for which several grain-size fractions of phengite as well as omphacite, glaucophane, calcite and clinozoisite were separated and analyzed (see **Table A3** for the full analytical dataset). The large spread in Rb/Sr ratios for the different white mica fractions **(**Fig. 10**)** is most probably largely due to difficulties in separating the white mica from clinozoisite, the latter being very rich in Sr. No obvious correlation is visible between white mica grain size and apparent age; hence the white mica population appears homogeneous in its age signature.

An isochron corresponding to an age of 41.59 ± 0.73 Ma has been obtained **(**Fig. 10**).** The high MSWD of 559 does not affect the age information as it is largely due to Sr-isotopic disequilibria between the low-Rb/Sr phases. Omphacite has the lowest time-corrected ^{87}Sr/^{86}Sr ratio, which suggests that some of the omphacite may be slightly older

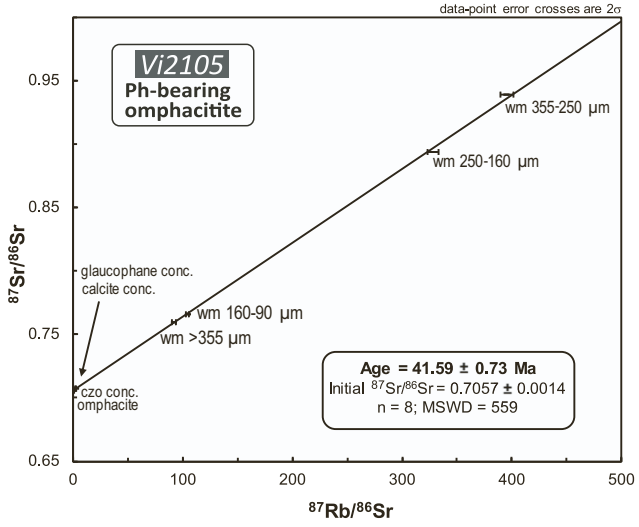

Fig. 10. Multi-mineral Rb-Sr isochron for the omphacitite sample Vi2105.

than the other phases (namely clinozoisite – formed during lawsonite breakdown – and calcite).

8. Thermodynamic modelling insights on elemental mobility

Deciphering a metasomatic process requires the identification of the chemical elements involved in mass transfer. The omphacitization of a jadeitite was already studied by García-Casco et al., (2009), though not from a thermodynamic point of view. However, pseudosection modelling of jadeite is challenging and did not yield any satisfactory results, so we focus here on the metasomatic processes forming an omphacitite from an eclogite. A classical method used in metasomatic rock studies is a mass balance calculation (see **Fig.S7** for more details). In our case, no element could be identified as immobile with certainty, including elements with a typically low mobility like HFSEs, and changes in the total mass or volume are unknown. Even though the assumption of immobile elements or of a certain volume change may lead to misinterpretation of the elemental behaviors during metasomatic processes, the significantly low iron content in omphacitite compared to Fe-Ti-Eclogite points to a probable Fe-loss during metasomatism. To quantify the role of iron in mineralogical changes and to assess the role of other elements we performed thermodynamic modelling using the software PerpleX (version 6.9.0, Connolly, 2005). We modelled the effect of independent changes in the chemical potentials of several elements, a method that was previously shown as relevant for metasomatic rocks (*e.g* Angiboust et al., 2014). The chemical potential μ_X of the component X is an intensive variable representing changes in the Gibbs energy of the system (G) upon changes in moles of X (n_X). The chemical potential μ_X is thus the conjugate variable of the extensive variable n_X. When local equilibrium is reached at the equilibrium volume scale (herein comprising the protolith rock and the infiltrating fluid), the chemical potential of a given component X has the same value at every point of the system. This involves compositional changes (n_X) by transfer of matter between the different phases (Powell et al., 2019; Tursi, 2022). In the following models, elements whose mass percentage is fixed are considered as inert (Korzhinskii, 1959) and their chemical potentials are internally buffered (Evans et al., 2013) while the other elements are considered as perfectly mobile or externally buffered, which means that their chemical potentials are controlled by the incoming fluid.

Pseudosections were calculated using the thermodynamic dataset of Holland and Powell (2011) associated with the following activity models for solid solutions: omphacite (Green et al., 2016), garnet (White et al., 2014), clinoamphibole (Green et al., 2016), chlorite (White et al., 2014) and the ideal Fe-Mg solution for talc. The chemical system is NCFMASH (water saturated) with the fluid considered as pure H_2O. The pressure and temperature were fixed at near peak (early retrograde) conditions (P = 2.5 GPa, T = 550 °C) assuming that metasomatism occurred close to peak metamorphism. The consistency between modelling and observations also served as a test for this assumption. Ferric iron, which is relatively low in omphacite (XAeg <10), has been neglected for the sake of simplification. The addition of subtle amounts of ferric iron would have slightly shifted the phase assemblage boundaries and expanded the stability fields of Fe^{3+}-bearing solution models (*i.e.,* clinoamphibole and omphacite), but the relative positions of the calculated phase assemblages would not change. However, not considering ferric iron prevents any inference concerning the reducing or oxidizing conditions induced by the metasomatic fluids. We first modelled a decrease in μ_{FeO} following the mass-balance results (**Fig.S7a**, Fig. 11a). The iron concentration is first buffered by garnet and remains relatively constant upon decreasing μ_{FeO}. The buffering effect disappears as soon as garnet starts to be consumed, and the FeO wt% drops sharply from ~13 wt% to ~2.5 wt% thus reaching the low Fe content of an omphacitite. The disappearance of garnet is associated with the formation of lawsonite (as seen in most omphacitites; Fig. 6e,f), and in line with dissolved garnet fragments in some omphacitite samples (Fig. 6a, b). This first model shows that μ_{FeO} exerts a strong control on garnet

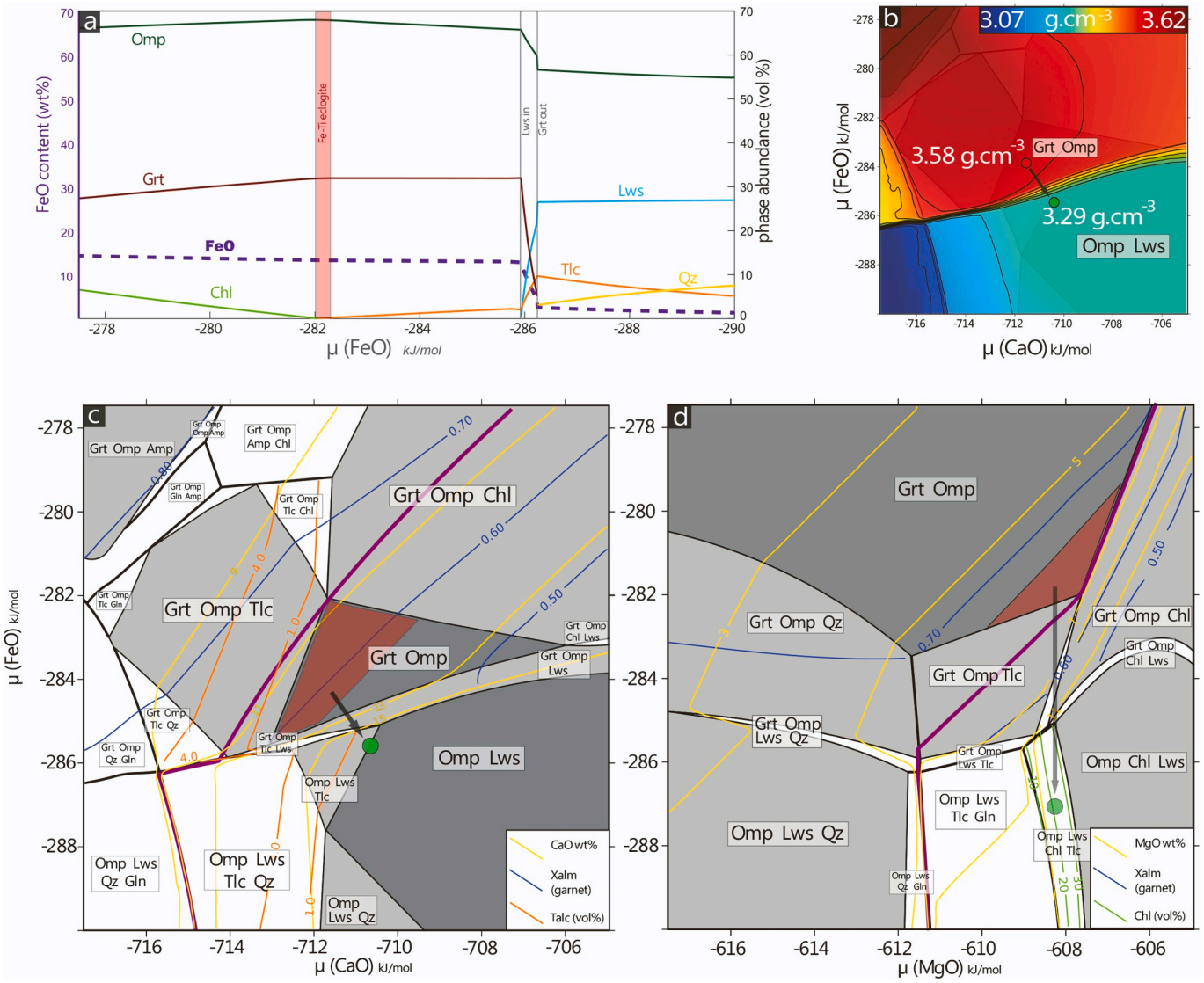

Fig. 11. Thermodynamic modelling of metasomatism in the NCFMASH system, starting from an average Fe-Ti eclogite composition (from Spandler et al., 2011) (a) Evolution of mineral modes and FeO wt% along the μ_{FeO} profile at fixed composition for the other elements and at fixed PT conditions (2.5 GPa, 550 °C). (b) Density variation in a μ_{CaO} - μ_{FeO} chemical potential diagram. (c) μ_{CaO} - μ_{FeO} diagram showing an omphacite-lawsonite field, and isopleths representing CaO wt%, talc mode and Xalm in garnet. The red field corresponds to the initial eclogite composition. Fields are colored depending on the variance V of the mineral assemblage (white: V = 2; light grey: V = 3; dark grey: V = 4). (d) μ_{MgO} - μ_{FeO} diagram illustrating the formation of chlorite, and isopleths representing MgO wt%, chlorite mode and Xalm in garnet. (For interpretation of the references to colour in this figure legend, the reader is referred to the web version of this article.)

stability when it reaches a low enough value, imposed by a fluid initially in strong disequilibrium with the rock. However, considering Fe as the only externally buffered element during omphacitization does not account for all the observations. Quartz formation is predicted along with an amount of talc that is slightly higher than observed. The variations in the chemical potentials of other elements were tested by the construction of μ - μ diagrams, associating iron with CaO, MgO (Fig. 11c,d), Na_2O or Al_2O_3 (**Fig.S7d,e**). The μ_{FeO} - μ_{CaO} diagram shows the appearance of an Omp-Lws-Tlc trivariant field and an Omp-Lws quadrivariant field when μ_{CaO} remains relatively constant during the decrease of μ_{FeO}, which implies a small increase in the CaO concentration. On the contrary, the first model (Fig. 11a and represented along the thick purple line in Fig. 11c) involves a fixed concentration in CaO along with a decrease in μ_{CaO}. These results show that calcium was not totally immobile during metasomatism and the fluid-rock interactions likely impacted the composition in calcium, but with a mixed behaviour between external and internal control explaining the small concentration increase and an almost constant chemical potential. MgO, NaO and Al_2O_3 are inferred to have a behaviour similar to CaO (in an opposite direction for Al_2O_3) thus explaining the difficulty to find immobile elements for mass-balance analysis. The case of MgO is interesting as a moderate increase in its chemical potential relative to the perfect immobility case (purple line) leads to the formation of Mg-chlorite (clinochlore), which fits the observation of clinochlore-rich omphacitite in Barant (Fig. 3h). Note that many of the metasomatic assemblages observed in natural samples and obtained by modelling are bimineralic (Omp + Lws) or trimineralic (Omp + Lws + Tlc), meaning that the degree of freedom in the associated stability field is greater than two (respectively four and three). It follows that these assemblages are not strictly constrained by variations in the two chosen mobile components, as other variables may vary within a given stability field.

Density change during metasomatism was also investigated and is presented in the μ_{FeO} - μ_{CaO} diagram (Fig. 11b). As expected, the disappearance of garnet leads to a significant decrease of the solid density during the omphacitization of an eclogite (from ~3.58 g.cm^{-3} to 3.29 g.cm^{-3}). The impact of this evolution on fluid ingression and

metasomatic processes is discussed in section 9.3.2.

9. Discussion

A summary of the proposed mineralogical evolution of the studied samples is depicted in Fig. 12, where we reconstruct the inferred metamorphic history based on the textures and mutually overprinting mineral assemblages.

9.1. New constraints on the origin of the Monviso jadeitite

The finding of a new jadeitite-omphacitite occurrence provides a better insight into the petrological and geochemical diversity of Monviso jadeitites, which is crucial for improving the understanding of the jadeitite-forming processes. A better knowledge of this diversity may also have archeological implications as jadeitites and omphacitites were used during the Neolithic period in W. Europe as a material of choice for producing polished stone axeheads. They were exchanged by prehistoric communities and travelled across the entire continent (*e.g.* Pétrequin et al., 2011). It is now well-accepted that the largest European source of the raw material used for these axes was the Monviso meta-ophiolite but petrological data are still limited.

Jadeitite and omphacitite are commonly found as decimeter to meter-sized boulders in quaternary alluvial and morainic deposits in the upper Po valley (Bulè, Porco, Rasciassa localities; *e.g.* Compagnoni et al., 2007; Forno et al., 2015). While it is likely that the host material that originally encapsulates the jadeitites (and the associated eclogites) is serpentinite from the basal serpentinite unit (Compagnoni et al., 2012; Compagnoni and Rolfo, 2003), further evidence for *in situ* observation of the jadeitite-serpentinite contact was scarce. The finding of an *in situ* block of jadeitite in the Intermediate Shear Zone, *i.e.* in a structural position very distinct from the previously reported jadeitite bodies several kilometers further south in the serpentinite basal unit of the massif (Figs.1 and 2; Compagnoni and Rolfo, 2003), yields important information on the genesis of jadeitites. Based on previous petrological and geochemical observations, it is suggested that the jadeitite bodies correspond to former plagiogranite dykes that were fully replaced during the alpine subduction event (replacement, "R-type", according to the Tsujimori and Harlow, 2012 classification). Our zircon age data yielded upper Jurassic ages (c.150 Ma), thus supporting the previously proposed hypothesis that Monviso jadeitites derive from the partial to full replacement of a former plagiogranite body emplaced during formation of the Tethyan oceanic lithosphere (identical within uncertainty to the 152 Ma U-Pb zircon age obtained by Lombardo et al., 2002; Fig. 9b). No relict mineral phase from this magmatic stage has been preserved in the studied sample with the notable exception of zircon, which displays widespread dissolution features.

The most pristine record of the potential protolith has been described in Lombardo et al. (2002) and Castelli and Lombardo (2007) in the southern part of the Monviso meta-ophiolite, where a Jurassic meta-plagiogranite body has been partly eclogitized as indicated by the growth of jadeite crystals. A well re-equilibrated metaplagiogranite is described in Compagnoni et al. (2012) who report a Qtz-Jd bearing block core and a rim of relatively dark jadeitite. However, our jadeitite substantially differs from the ones previously studied. Regarding the presence of phengite, the measured whole-rock concentration of K_2O spans a similar range as the available plagiogranite data from the literature (Fig. 8). Yet, our jadeitite sample does not match the trace element signature of most alpine plagiogranite bodies (Fig. 8): this discrepancy can either be explained by intense fluid-rock interactions leading to the loss of the initial geochemical signature, or by a different protolith composition. The fine-scale omphacitization, well visible along jadeite grain boundaries (Fig. 4a, see also section 9.2), provides evidence for fluid-related re-equilibration of the chemical composition of this rock (Fig. 13a,b). However, for trace elements the jadeitite composition is not intermediate between the plagiogranites and the omphacite (Fig. 8), as expected if the plagiogranite signature was lost during the omphacitizing event. The chemical changes may also have occurred before omphacitization, during jadeitization or a subsequent event. Indeed, the studied jadeitite must have undergone substantial metasomatism during jadeitization of the plagiogranite since the SiO_2 normally released during jadeitization of a quartz- and albite-bearing rock has seemingly been fully washed out (because no free quartz was found). This raises the possibility that some jadeitization mechanisms may differ from those reported by Compagnoni et al. (2012). Alternatively, the plagiogranitic protolith may have had a different composition than the plagiogranites reported elsewhere in the Alps, perhaps as a consequence of seafloor hydrothermal alteration. The geochemical variability of plagiogranites in oceanic settings was demonstrated by Freund et al. (2014) but a depletion in HREE is not typical, and little

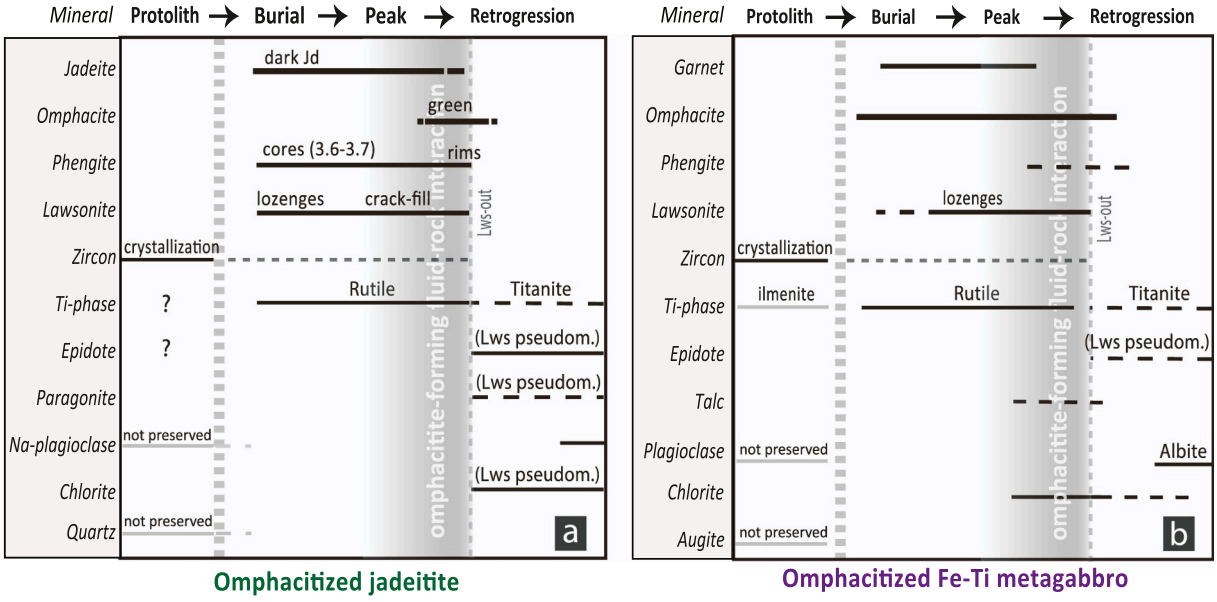

Fig. 12. Summary of observed paragenetic sequences during metasomatism affecting both the jadeitite (a) and the Fe-Ti metagabbro (b). Note that the three stages identified in section 9.3.1 cannot be distinguished and are gathered within the thickness of the grey-shaded band on panel b. pseudom.-pseudomorph.

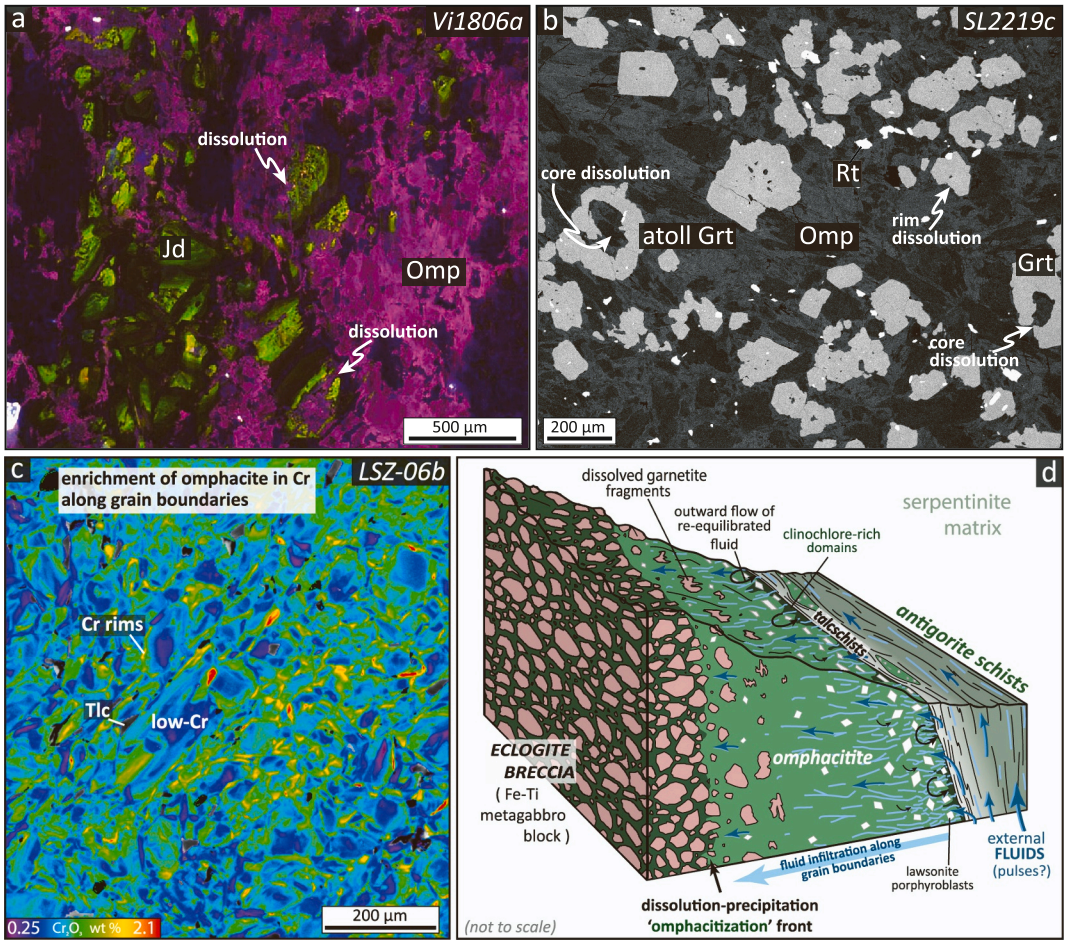

Fig. 13. (a) Cathodoluminescence image of the boundary between the jadeitite Vi1806a and its omphacitized region. Green-shaded jadeite cores exhibit corrosion of their cores and associated replacement by a CL purple-shaded omphacitic pyroxene. Note the atoll structure well visible in the dissolved crystal from the bottom part of this image. (b) BSE image showing how a garnetite band from an Fe-Ti metagabbro becomes replaced by omphacite during the metasomatic process as shown by the formation of atoll garnet and by the corrosion of outer garnet rims. (c) X-ray map of the Cr_2O_3 (wt%) content in metasomatic sample LSZ-06b showing the enrichment of omphacite in Cr along grain boundaries, illustrating the consequences of the passage of the metasomatic replacement front. (d) Schematic sketch summarizing formation processes and the structural relationships between the different lithologies visible around a brecciated Fe-Ti metagabbro block. (For interpretation of the references to colour in this figure legend, the reader is referred to the web version of this article.)

variability has been reported so far for alpine plagiogranites. We therefore speculate that both mechanisms, namely a slightly different protolith composition and fluid-rock interactions during subduction, could explain the bulk-rock composition change of the jadeite - omphacite block from Rocce Alte locality.

9.2. *Timing and PT conditions of omphacitization*

The P-T-t history of the studied blocks rimmed by omphacitite is well-constrained as they are part of the extensively studied Lago Superiore Unit. They were first buried through the blueschist facies down to the lawsonite-eclogite facies at c. 45 Ma (Groppo and Castelli, 2010; Angiboust et al., 2012; Rubatto and Angiboust, 2015; Fig. 1b). Later, the entire meta-ophiolitic sliver was coherently exhumed through the epidote-blueschist facies (at near 37 Ma) leading to partial re-equilibration of some of the weakest lithologies (*e.g.* metasediments and metabasalts above the ISZ, serpentinites from the LSZ; Angiboust and Glodny, 2020; Gilio et al., 2020). Petrographic relationships on both localities enable to bracket the timing of omphacitization and indicate that (i) high-Si phengite formation pre-dates omphacite crystallization in the jadeitite, (ii) that high-Si phengite was deformed during the mylonitization of the omphacitized jadeitite block rim (Fig. 4d, Fig. 5c) and (iii) that lawsonite was formed ubiquitously during the studied deep-seated metasomatic processes, filling cracks or growing associated with omphacite in variably strained domains (Fig. 2d,e,5c). Therefore, we demonstrate that the omphacitization process documented here occurred in a narrow PT range in the lawsonite-eclogite facies, between 2.5 and 2.0 GPa and between 45 Ma (peak burial age) and 42 Ma (our new Rb-Sr age on the mylonitized omphacitite; see P-T-t path). Since no Alpine zircon rims thicker than twenty micrometers (*i.e.* suitable for U-Th-Pb SHRIMP dating) were found during thin section observation and mineral separation, it is not possible to date with greater accuracy the age of the omphacitization event. The corroded appearance of zircon crystals (Fig. 9) as well as the scarcity of inferred alpine metamorphic zircon rims (see **Fig.S2e**) suggest that little to no zircon precipitation occurred during the metasomatic replacement. This is in contrast with the observation of newly formed zircon crystals identified in omphacite crack-seal veins in the Lago Superiore Metagabbro nearby (Rubatto and Hermann, 2003), suggesting different Zr behaviors in metamorphic fluids between closed and open systems (see Spandler et al., 2011). We can thus speculate that the c. 45 Ma U-Th-Pb zircon age obtained by Rubatto and Angiboust (2015) on Monviso Fe-Ti metagabbro eclogite breccias relates more to the age of the brecciation event than to the age of block rind fluid-rock interaction.

9.3. Metasomatic processes and fluids composition

9.3.1. Multiple events of overprinting metasomatism and evolution of fluid chemistry

Metasomatic rind formation is documented around the blocks and lenses embedded in the Lower Shear Zone (Angiboust et al., 2014; Locatelli et al., 2019; Hoover et al., 2022; Fig. 13d). Garnet displays chemical oscillations, with Cr- richer annuli (Fig. 7b), and omphacite exhibits chromium enrichments along its grain boundaries (Fig. 13c). Lawsonite formed during this metasomatic event is also substantially enriched in chromium (Fig. 6f), as already noted by Angiboust et al. (2014). This event, hereafter named '*stage I event*', is interpreted as the result of the interaction between the block and serpentinite-derived fluids with variable sediment signature contamination (Angiboust et al., 2014). Note that the Rocce Alte jadeitite (that belongs to the Intermediate Shear Zone) does not seem to have significantly undergone this metasomatic event, as indicated by its low Cr content.

Our new observations enable the identification of a subsequent metasomatic event (hereafter named *stage II event*) characterized by (i) dissolution of the oscillatory *stage I* Cr-bearing garnet and replacement by a discrete Cr-poor garnet overgrowth (Fig. 6a,b,c,d); (ii) dissolution-precipitation processes of the prograde jadeite in the jadeitite sample (Fig. 4c; Fig. 13a) and the replacement of *stage I* omphacite in LSZ metasomatites by a low-Cr omphacite generation (Fig. 6a,b); and (iii) partial dissolution of the magmatic zircon in both types of omphacitite (Fig. 9). At the block scale, rounded garnetite fragments (inherited from the eclogite breccia) are embedded in a *stage II* omphacitite-dominated matrix and exhibit incipient dissolution and replacement by coarse-grained omphacite (Fig. 3c; Fig. 7a; Fig. 13b,d). All these replacement features underline the extremely reactive and corrosive nature of the incoming fluids that generate this pervasive omphacitization event, including for lithologies as refractory as garnetites.

With all the caution needed when using rock paragenesis and chemistry for unravelling fluid composition, we infer, based on mineral and rock geochemistry as well as chemical potential thermodynamic modelling, that the reacting fluid leached some substantial amounts of iron from the rock volume, while the rock captured Ca and Mg from the fluid phase (Fig. 11). Fluids formed by serpentinite dehydration are potentially oxidized (Maffeis et al., 2023) and may be highly corrosive for garnet, but no evidence for a major change of the redox state was found in the clinopyroxenes, thus discarding this process as the major driving force for omphacitization. Even though the source of the fluids responsible for the observed omphacitization cannot be directly assessed, the relatively Cr-depleted nature of *stage II* minerals suggests that serpentinite-derived fluids might have not been the dominant compound of the incoming fluid phase. The question of the source and chemistry of the fluids that precipitate jadeitite or omphacitite remains a matter of discussion in the community (*e.g.* Harlow et al., 2016; Sorensen et al., 2006). We note, based on mineralogy, whole rock chemistry and projections (Fig. 14), that the metasomatic alteration exchange vectors both for the jadeitite and the Fe-Ti metagabbro converge towards a relatively restricted domain, close to an omphacite composition (green spots in Fig. 14). The bulk of the omphacite crystallizes during this *stage II event*, that therefore represents a major contributor to the omphacitization sequence herein described. A last event (hereafter named *stage III*) texturally post-dates *stage II* features and is characterized by the local formation of a clinochlore ± lawsonite ± omphacite ± rutile/ilmenite ± sulphides along fractures zones and block outer rims (Fig. 3h, Fig. 13d, **Fig.S2b,c**). While the first two stages are of metasomatic origin, field and microscopic features (Fig. 3h, Fig. 6a,b) rather indicate that the *stage III* paragenesis formed by precipitation (and not replacement) from a fluid phase. The large amount of clinochlore (Mg-rich chlorite) forming during *stage III* strongly suggests an ultramafic signature for this late fluid infiltration event, even though the presence of rutile and ilmenite supports a mafic component. Overall, this sequence of (at least) three chemically distinct events denotes a complex evolution of the chemistry of the fluid reacting with Monviso shear zones block rims (Fig. 15), with two ultramafic sources bracketing a fluid-rock interaction event of unknown source, perhaps mafic-derived.

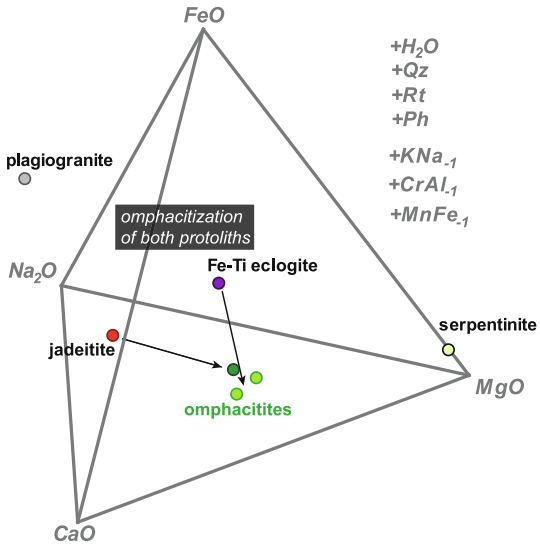

Fig. 14. Projection of the whole-rock compositions of the herein studied lithologies in a CaO-FeO-MgO-Na_2O tetrahedron projected from the phases and exchange vectors indicated. Plagiogranite composition is an average value from Castelli et Lombardo (2007) and Castelli et al. (2002), serpentinite is from Angiboust et al. (2014), Fe-Ti eclogite from Spandler et al. (2011), jadeitite is sample Vi1806a and omphacitites are samples Vi2105 (dark green), SL2219c and SL2220d (light green). Note the convergence of metasomatic alteration vectors to an omphacitite composition (green dots) for both the jadeitite (omphacitization along the exchange vector MgCaNa-2) and the Fe-Ti metagabbro, involving a significant Fe-loss. (For interpretation of the references to colour in this figure legend, the reader is referred to the web version of this article.)

The numerous omphacitite rinds or blocks found in other localities representing deeply subducted, serpentinized environments (*e.g* Bröcker and Keasling, 2006; Shigeno et al., 2012; Harlow, 1994; Tsujimori, 1997) highlight the general significance of the omphacitization process in these environments. Although this metasomatism likely results from similar chemical processes, it also implies that omphacitization occurs in a variety of subduction settings. It thus affects various protolith rocks subjected to different P-T conditions, potentially surrounded by slightly varying lithologies (though serpentinite-dominated) and fluid sources.

9.3.2. Textural record of fluid percolation processes

The studied rocks are characterized by widespread dissolution textures, at both macro and micro scales. The outer rims of metasomatized brecciated Fe-Ti eclogites host sparse garnetite fragments exhibiting dissolution and replacement by omphacite along their rims. Finger-shaped dissolution fronts corrode the inner part of some garnetite fragments (Fig. 7a, 13d). Similar replacement textures were described in the jadeite-omphacite block at hand specimen and microscopic scales (Fig. 4a, 13a). Atoll structures, widespread both in garnet and jadeite (Fig. 13b, **Fig.S4f,g**) in the reaction zones, reveal a strong thermodynamic disequilibrium between the incoming omphacitizing fluid and the previously formed mineral generation (*e.g.* Giuntoli et al., 2018; Hyppolito et al., 2019). These structures in the studied omphacitites cannot be explained by pure diffusive elemental exchange at the boundary between the eclogite, the jadeitite and the host ultramafic lithologies and thus involves an advective influx of a fluid phase.

While it is obvious that dissolution-precipitation processes occur in the metasomatized blocks, the issue of the physical mechanisms driving the fluid influx into the studied blocks requires careful examination. The apparent permeability contrast between the host serpentinite

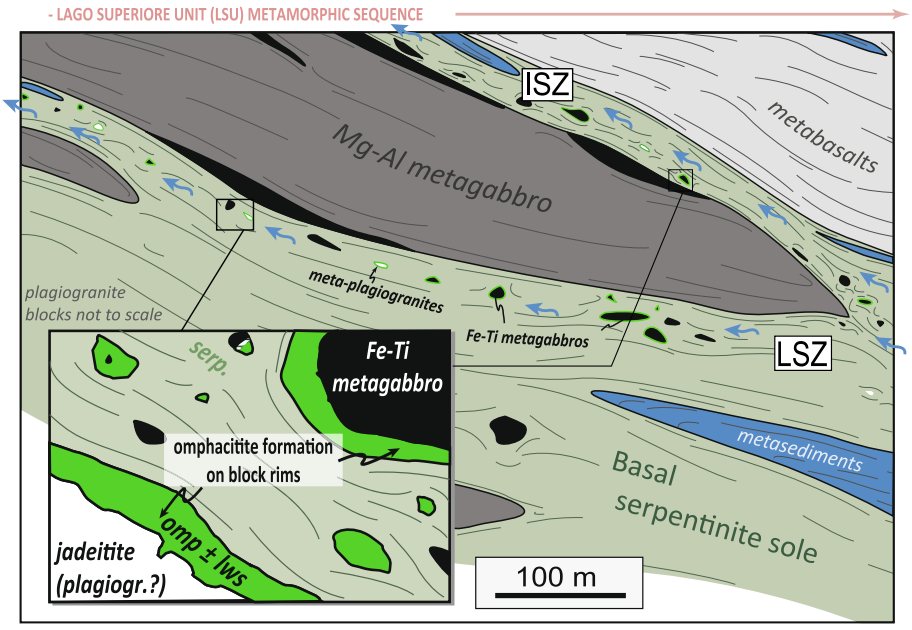

Fig. 15. Sketch locating the place of the studied blocks within the deeply subducted Lago Superiore Unit sequence in the lawsonite-eclogite facies when omphacitization-related metasomatism occurred. The interface-parallel fluid flux responsible for the studied metasomatic replacement infiltrated both the Intermediate Shear Zone (ISZ) and to a greater extent the Lower Shear Zone (LSZ). Inset: schematic, not to scale, view depicting the formation of a replacement front around jadeitite and Fe-Ti metagabbro blocks embedded within sheared antigorite serpentinites. Plagiogr.- plagiogranite; serp.- serpentinite.

(10^{-19}–10^{-22} m^2 in deformed antigoritite, Kawano et al., 2011; Ganzhorn et al., 2019) and the eclogite block ($<10^{-23}$ m^2: Angiboust and Raimondo, 2022) and a likely similar contrast between jadeitite and surrounding serpentinite would intuitively prevent any fluid flux towards the block core. A mechanism typically invoked for creating a transient high permeability is deformation. However, no evidence was found for shear-related stresses during the omphacitization process, as indicated by the apparent 'static' replacement visible in the jadeitite sample (Fig. 4a) and by the randomly oriented omphacite grains in omphacitites before mylonitization (Fig. 6a). We can therefore posit that tectonic shearing did not play a key role in enhancing fluid mobility and replacement processes along block rinds. Transient brittle fracturing is an efficient mechanism for opening fluid pathways in subduction zones (*e.g.* Muñoz-Montecinos and Behr, 2023) and, under certain circumstances this mechanism does not necessarily require tectonic stresses as it may arise from reaction-driven volume changes (Jamtveit et al., 2009). While no major volume change is expected in the omphacitization process starting from a jadeitite (similar density), this parameter cannot be determined accurately for the omphacitization of the eclogite because of a significant mass transfer that may affect the volume variation (see section 8, Fig. 11b and **Fig.S7**). In addition, because both jadeitite and eclogite-breccia protoliths are mostly anhydrous and thus unlikely to release metamorphic fluids at near peak conditions, an internal build-up of pore fluid pressure leading to block-scale hydrofracturing can be discarded, as suggested by the absence of crack-seal features and vein networks in both lithologies. The lack of brittle structures that could potentially enhance permeability suggests that the metasomatic fluid percolated in a low permeability, though not totally sealed medium, probably using grain boundaries as pathways. This phenomenon fits our observations and was documented in previous investigations (Etheridge et al., 1983; Ganzhorn et al., 2019; Putnis and Austrheim, 2010; Zertani et al., 2022). The role of grain boundaries is particularly visible in the jadeitite and in the *stage I* metasomatized eclogite (Fig. 4a,c; Fig. 7b; Fig. 13c), while extensive fluid-rock interactions may have obliterated the evidence of this process in metasomatites with the most extensive imprint. The observed replacement along grain boundaries typically occurs on a width of 10–100 μm but is unlikely to represent a single fluid ingression event as the grain boundary thickness (representing porosity between grains) in high pressure rocks is estimated to be at the nanometer scale (Chogani and Plümper, 2023; Ganzhorn et al., 2019). This suggests that metasomatism proceeded *via* numerous, incremental events showing the maintenance of those fluid pathways over a certain period of time. This idea of a periodicity in the fluid flux is supported by garnet and omphacite inner oscillatory structures (Fig. 6b; Fig. 7b) that potentially witness individual influx events (Angiboust et al., 2014; see also Hoover et al., 2022, 2023 and García-Casco et al., 2009) even though the timing of each fluid-rock interaction cannot be determined with current *in situ* geochronological methods.

Once established that grain boundaries represent efficient pathways for fluid ingress and preferential loci for the studied dissolution-precipitation process, questions remain about the physical nature of processes driving the nearly complete replacement of the jadeitite or the eclogite. The issue of fluid fluxes through low permeability rocks was addressed by Putnis and Austrheim (2010), who use interface coupled dissolution-precipitation (ICDP) to explain the crystal replacement *via* transient porosity generation, subsequent permeability creation and associated fluid ingress. Under these highly compacted conditions, any external fluid influx will render the system mechanically unstable through enhanced micro-hydrofracturing, potentially along grain boundaries (Connolly, 2010; Putnis and Austrheim, 2010). Such 'porosity-wave'- like mechanisms, known from geophysical studies (Skarbek and Rempel, 2016), have been invoked to account for complex and poly-phased fluid-rock interaction events recorded in deep-seated metamorphic rocks (see for instance Taetz et al., 2018 and Muñoz-Montecinos et al., 2021 for other field examples). We can thus suggest that a mixed ICDP-porosity wave mechanism has enabled the metasomatic overprint visible in the studied blocks (Fig. 13d, Fig. 15) and more generally in a large variety of metasomatic rocks from various block-in-matrix mélange settings worldwide (*e.g.* Bebout and Penniston-Dorland, 2016; Gyomlai et al., 2021; Shigeno et al., 2012).

9.4. Omphacitite records subduction deformation history

Deformation patterns in exhumed jadeitites/omphacitites can yield (i) important information on differential stress levels in deep subduction environments (Angiboust et al., 2021; Piepenbreier and Stöckhert, 2001) and (ii) provide anchor points to constrain the relative timing of fluid-rock interaction. While at the Barant locality omphacitite appears relatively undeformed with randomly-oriented, coarse-grained crystals (Fig. 3c), the omphacitized jadeitite from Rocce Alte has been moderately to intensely strained after omphacitization (Fig. 2e, Fig. 5c), with a Rb-Sr end of deformation age estimated at c. 42 Ma attributed to early exhumation (Fig. 10, Fig. 15). We thus interpret the 42 Ma age as marking the end of a deformation event that occurred along block rim upon exhumation, around 3 to 4 Myr after peak burial conditions in the 1.8–2.0 GPa window as the sample was leaving the lawsonite stability field (Fig. 1b). Interestingly, no significant differences can be noted in the exhumation rates between the upper and the lower parts of the high-pressure exhumation path (Fig. 1b), with rather constant decompression rates on the order of 0.15 GPa/Ma. This observation confirms the inferences from Angiboust and Glodny (2020) suggesting that the exhumation of the Monviso meta-ophiolite was decoupled from the underlying Dora Maira complex, for which exhumation rates strongly decrease during exhumation as noted by Rubatto and Hermann (2001) (see also Bonnet et al., 2022).

At the microscopic scale, EBSD mapping in fine-grained omphacitite reveals a clear crystallographic preferred orientation (CPO) where the strongest fabric corresponds to the (001) poles aligned parallel to the macroscopic lineation (Fig. 5d), typically interpreted as resulting from a stronger contribution of non-coaxial deformation (L-type tectonites; *e.g.*, Keppler, 2018). The formation of a CPO can stem from two main different mechanisms (dislocation creep, which involves crystal plasticity, and/or diffusion creep) that may act concomitantly (Godard and van Roermund, 1995; McNamara et al., 2024). Indeed, some truncated omphacite crystals visible in the maps (Fig. 5d) suggest the presence of pressure-solution processes during mylonitization, while subgrain rotation can be identified in the misorientation map (**Fig.S4**). The relative roles of deformation mechanisms may be challenging to infer and their detailed identification is out of the scope of this study. Nevertheless, some features including a strong fine-grained foliation, irregular grain boundaries and a few sub-grain boundaries suggest that deformation in these omphacitites rinds was partly (but not exclusively) accommodated by crystal plasticity, as proposed for similar rocks by Bascou et al., (2001). Although the experimentally-derived flow laws may only provide an upper-bound for the mechanical strength of omphacitites, this raises questions regarding the stress levels required to enable plastic flow of omphacitites. The flow laws established for omphacite (Zhang et al., 2006, extrapolated at LT-conditions) and jadeite (Orzol et al., 2006) indicate a viscosity $>10^{20.5}$ Pa.s (values calculated for 500 °C and an average shear zone strain rate of 10^{-11} s^{-1}). This value is several orders of magnitude greater than the viscosities estimated for the encapsulating serpentinites (10^{17} Pa.s; Hilairet et al., 2007). Given the viscosity difference, it seems unlikely to develop such foliation in omphacitites. We therefore speculate that either the serpentinite schists observed in the ISZ are stronger than expected, or the contribution of pressure-solution creep in clinopyroxene substantially reduces its mechanical strength (Godard and van Roermund, 1995; McNamara et al., 2024). Stress distribution heterogeneities at the hectometer to kilometer- scale could have also played an important role as indicated by the absence of mylonitization in the omphacitite rims of the Barant blocks. In any case, further experimental data are required to refine rheological parameters for metasomatic rocks, particularly for such monomineralic clinopyroxenites that could represent potential targets for the elaboration of new paleopiezometers.

10. Conclusions

Jadeitite and omphacitite occasionally occur in and around tectonic blocks along serpentinite-bearing shear zones in the Monviso Lago Superiore Unit. The finding of middle-Jurassic age zircon crystals in both jadeitites and omphacitites indicates that these two rock types formed *via* metasomatic replacement of previous meta-igneous bodies. While it is likely that jadeitites formed after oceanic Tethyan plagiogranites, our field observations reveal that omphacitite is observed (i) replacing jadeitite and (ii) forming a well-marked reaction front around brecciated, eclogitized Fe-Ti metagabbro blocks that are common in Monviso massif eclogite-facies shear zones. Petrochronological data suggests that this omphacitization event occurred upon early exhumation in the lawsonite-eclogite facies in the 42–45 Ma window. The replacement of an eclogitic paragenesis by a lawsonite-omphacite assemblage can be thermodynamically modelled, mostly by decreasing the chemical potential of iron. We have shown that omphacitization appears as a common process in serpentinite-bearing eclogite-facies shear zones as a consequence of the infiltration of far-travelled fluids in thermodynamic disequilibrium with the reacting block rim. The dissolution-precipitation textures documented here highlight the highly reactive nature of such fluids and their capacity to pervasively replace previous assemblages, including in low-permeability rocks such as garnet-rich eclogites or jadeitites.

CRediT authorship contribution statement

Clothilde Minnaert: Investigation, Writing – original draft, Writing – review & editing, Methodology, Visualization. **Samuel Angiboust:** Conceptualization, Funding acquisition, Investigation, Writing – original draft, Writing – review & editing, Methodology, Visualization. **Aitor Cambeses:** Investigation, Writing – original draft, Methodology. **Johannes Glodny:** Investigation, Methodology, Writing – original draft. **Jesús Muñoz-Montecinos:** Investigation, Writing – original draft, Methodology. **Antonio Garcia-Casco:** Investigation, Writing – review & editing, Software, Writing – original draft.

Declaration of competing interest

The authors declare that they have no known competing financial interests or personal relationships that could have appeared to influence the work reported in this paper.

Acknowledgements

Stephan Borensztajn, Michel Fialin, Nicolas Rividi and Clémentine Fellah are warmly acknowledged for assistance with SEM and probe data acquisition. We also thank Noah Collin and Helie Peyron for assistance in the field and Bruno Reynard for insightful discussion. JMM acknowledges W. Behr for funding and L. Morales for assistance during EBSD analysis. Field and analytical costs were covered by an internal ENS de Lyon grant to SA. This is IBERSISMS publication #114.

Appendix A. Supplementary data

Supplementary data to this article can be found online at https://doi.org/10.1016/j.lithos.2024.107738.

References

Angiboust, S., Glodny, J., 2020. Exhumation of eclogitic ophiolitic nappes in the W. Alps: New age data and implications for crustal wedge dynamics. Lithos 356, 105374.
Angiboust, S., Raimondo, T., 2022. Permeability of subducted oceanic crust revealed by eclogite-facies vugs. Geology 50 (8), 964–968.
Angiboust, S., Agard, P., Raimbourg, H., Yamato, P., Huet, B., 2011. Subduction interface processes recorded by eclogite-facies shearzones (Monviso, W. Alps). Lithos 127 (1–2), 222–238.

Angiboust, S., Langdon, R., Agard, P., Waters, D., Chopin, C., 2012. Eclogitization of the Monviso ophiolite (W. Alps) and implications on subduction dynamics. J. Metamorph. Geol. 30 (1), 37–61.
Angiboust, S., Pettke, T., De Hoog, J.C., Caron, B., Oncken, O., 2014. Channelized fluid flow and eclogite-facies metasomatism along the subduction shear zone. J. Petrol. 55 (5), 883–916.
Angiboust, S., Muñoz-Montecinos, J., Cambeses, A., Raimondo, T., Deldicque, D., Garcia-Casco, A., 2021. Jolts in the Jade factory: a route for subduction fluids and their implications for mantle wedge seismicity. Earth Sci. Rev. 220, 103720.
Balestro, G., Fioraso, G., Lombardo, B., 2011. Geological map of the upper Pellice Valley (Italian Western Alps). J. Maps 7 (1), 634–654.
Bascou, J., Barruol, G., Vauchez, A., Mainprice, D., Egydio-Silva, M., 2001. EBSD-measured lattice-preferred orientations and seismic properties of eclogites. Tectonophysics 342 (1–2), 61–80.
Bebout, G.E., Penniston-Dorland, S., 2016. Fluid and mass transfer at subduction interfaces - the field metamorphic record. Lithos 240-243, 228–258.
Bebout, G.E., Agard, P., Kobayashi, K., Moriguti, T., Nakamura, E., 2013. Devolatilization history and trace element mobility in deeply subducted sedimentary rocks: Evidence from Western Alps HP/UHP suites. Chem. Geol. 342, 1–20.
Bonnet, G., Chopin, C., Locatelli, M., Kylander-Clark, A.R., Hacker, B.R., 2022. Protracted Subduction of the European Hyperextended Margin Revealed by Rutile U-Pb Geochronology Across the Dora-Maira Massif (Western Alps). Tectonics 41 (4), e2021TC007170.
Bröcker, M., Keasling, A., 2006. Ionprobe U-Pb zircon ages from the high-pressure/low-temperature mélange of Syros, Greece: Age diversity and the importance of pre-Eocene subduction. J. Metamorph. Geol. 24 (7), 615–631.
Castelli, D., Lombardo, B., 2007. The plagiogranite-FeTi-oxide gabbro association of Verne (Monviso metamorphic ophiolite, western Alps). Ofioliti 32 (1), 1–14.
Castelli, D., Rostagno, C., Lombardo, B., 2002. Jd-Qtz-bearing metaplagiogranite from the Monviso meta-ophiolite (Western ScambelluriAlps). Ofioliti 27 (2), 81–90.
Chogani, A., Plümper, O., 2023. Decoding the nanoscale porosity in serpentinites from multidimensional electron microscopy and discrete element modelling. Contrib. Mineral. Petrol. 178 (11), 78.
Compagnoni, R., Rolfo, F., 2003. First report of jadeitite from the Monviso meta-ophiolite, Western Alps. In: GEOITALIA, 4° forum FIST. FIST, pp. 205–206.
Compagnoni, R., Rolfo, F., Manavella, F., Salusso, F., 2007. Jadeitite in the Monviso meta-ophiolite, Piemonte zone, Italian western Alps. Periodico di Mineralogia 76 (2), 79–89.
Compagnoni, R., Rolfo, F., Castelli, D., 2012. Jadeitite from the Monviso meta-ophiolite, western Alps: occurrence and genesis. Eur. J. Mineral. 24 (2), 333–343.
Connolly, J.A., 2005. Computation of phase equilibria by linear programming: a tool for geodynamic modeling and its application to subduction zone decarbonation. Earth and Planetary Science Letters 236 (1–2), 524–541.
Connolly, J.A., 2010. The mechanics of metamorphic fluid expulsion. Elements 6 (3), 165–172.
Etheridge, M.A., Wall, V.J., Vernon, R.H., 1983. The role of the fluid phase during regional metamorphism and deformation. J. Metamorph. Geol. 1 (3), 205–226.
Evans, K.A., Powell, R., Frost, B., 2013. Using equilibrium thermodynamics in the study of metasomatic alteration, illustrated by an application to serpentinites. Lithos 168-169, 67–84.
Flores, K.E., Martens, U.C., Harlow, G.E., Brueckner, H.K., Pearson, N.J., 2013. Jadeitite formed during subduction: in situ zircon 671 geochronology constraints from two different tectonic events within the Guatemala Suture Zone. Earth Planet. Sci. Lett. 371–672 (372), 67–81.
Forno, M.G., Avondetto, S., Groppo, C.T., Rolfo, F., 2015. The Quaternary succession of the Bulè and Alpetto valleys (Monviso Massif, Piedmont) as a possible supply for prehistoric jade axes raw material. Rendiconti Lincei 26 (4), 425–432.
Franchi, S., 1900. Sopra alcuni giacimenti di roccie giadeitiche nelle Alpi Occidentali e nell'Appennino ligure. Bollettino Del Comitato Geologico D'italia 31, 119–158.
Freeman, S.R., Butler, R.W.H., Cliff, R.A., Rex, D.C., 1998. Dating mylonite evolution: a Rb–Sr and K–Ar study of the Moine mylonites. J. Geol. Soc. Lond. 155, 745–758.
Freund, S., Haase, K.M., Keith, M., Beier, C., Garbe-Schönberg, D., 2014. Constraints on the formation of geochemically variable plagiogranite intrusions in the Troodos Ophiolite, Cyprus. Contrib. Mineral. Petrol. 167, 1–22.
Ganzhorn, A.C., Pilorgé, H., Reynard, B., 2019. Porosity of metamorphic rocks and fluid migration within subduction interfaces. Earth Planet. Sci. Lett. 522, 107–117.
García-Casco, A., Rodríguez Vega, A., Cárdenas Párraga, J., Iturralde-Vinent, M.A., Lázaro, C., 2009. A new jadeitite jade locality (Sierra del Convento, Cuba): first report and some petrological and archeological implications. Contrib. Mineral. Petrol. 158 (1), 691 1-16.
Gilio, M., Scambelluri, M., Agostini, S., Godard, M., Pettke, T., Agard, P., Locatelli, M., Angiboust, S., 2020. Fingerprinting and relocating tectonic slices along the plate interface: evidence from the Lago Superiore unit at Monviso (Western Alps). Lithos 352, 105308.
Giuntoli, F., Lanari, P., Engi, M., 2018. Deeply subducted continental fragments: I. Fracturing, dissolution-precipitation and diffusion processes recorded by garnet textures of the central Sesia Zone (Western Italian Alps). Solid Earth 9, 167–189.
Glodny, J., Kühn, A., Austrheim, H., 2008. Diffusion versus recrystallization processes in Rb–Sr geochronology: isotopic relics in eclogite facies rocks, Western Gneiss Region, Norway. Geochim. Cosmochim. Acta 72 (2), 506–525.
Godard, G., van Roermund, H.L., 1995. Deformation-induced clinopyroxene fabrics from eclogites. J. Struct. Geol. 17 (10), 1425–1443.
Green, E., White, R.W., Diener, J., Powell, R., Holland, T., Palin, R., 2016. Activity–composition relations for the calculation of partial melting equilibria in metabasic rocks. J. Metamorph. Geol. 34 (9), 845–869.
Groppo, C., Castelli, D., 2010. Prograde P–T evolution of a lawsonite eclogite from the Monviso meta-ophiolite (Western Alps): dehydration and redox reactions during subduction of oceanic FeTi-oxide gabbro. J. Petrol. 51 (12), 2489–2514.
Gyomlai, T., Agard, P., Marschall, H.R., Jolivet, L., Gerdes, A., 2021. Metasomatism and deformation of block-in-matrix structures in Syros: the role of inheritance and fluid-rock interactions along the subduction interface. Lithos 386, 105996.
Harlow, G.E., 1994. Jadeitites, albitites and related rocks from the Motagua Fault Zone, Guatemala. J. Metamorph. Geol. 12 (1), 49–68.
Harlow, G.E., Tsujimori, T., Sorensen, S.S., 2015. Jadeitites and plate tectonics. Annu. Rev. Earth Planet. Sci. 43 (1), 105–138.
Harlow, G.E., Flores, K.E., Marschall, H.R., 2016. Fluid-mediated mass transfer from a paleosubduction channel to its mantle wedge: evidence from jadeitite and related rocks from the Guatemala Suture Zone. Lithos 258, 15–36.
Hertwig, A., McClelland, W.C., Kitajima, K., Schertl, H.P., Maresch, W.V., Stanek, K., Sergeev, S.A., 2016. Inherited igneous zircons 733 in jadeitite predate high-pressure metamorphism and jadeitite formation in the Jagua Clara serpentinite mélange of the Rio San Juan complex 734 (Dominican Republic). Contrib. Mineral. Petrol. 171, 1–26.
Hilairet, N., Reynard, B., Wang, Y., Daniel, I., Merkel, S., Nishiyama, N., Petitgirard, S., 2007. High-pressure creep of serpentine, interseismic deformation, and initiation of subduction. Science 318 (5858), 1910–1913.
Holland, T.J.B., Powell, R., 2011. An improved and extended internally consistent thermodynamic dataset for phases of petrological interest, involving a new equation of state for solids. J. Metamorph. Geol. 29 (3), 333–383.
Hoover, W.F., Penniston-Dorland, S., Baumgartner, L., Bouvier, A.S., Dragovic, B., Locatelli, M., Angiboust, S., Agard, P., 2022. Episodic fluid flow in an eclogite-facies shear zone: Insights from Li isotope zoning in garnet. Geology 50 (6), 746–750.
Hoover, W.F., Penniston-Dorland, S., Piccoli, P., Kylander-Clark, A., 2023. Reaction-Induced Porosity in an Eclogite-Facies Vein Selvage 743 (Monviso Ophiolite, W. Alps): Textural evidence and in Situ Trace elements and Sr Isotopes in Apatite. J. Petrol. 64 (1), 744 egac128.
Hyppolito, T., Cambeses, A., Angiboust, S., Raimondo, T., García-Casco, A., Juliani, C., 2019. Rehydration of eclogites and garnet- replacement processes during exhumation in the amphibolite facies. Geol. Soc. Lond. Spec. Publ. 478 (1), 217–239.
Inger, S., Cliff, R.A., 1994. Timing of metamorphism in the Tauern Window, Eastern Alps: Rb-Sr ages and fabric formation. J. Metamorph. Geol. 12 (5), 695–707.
Jamtveit, B., Putnis, C.V., Malthe-Sørenssen, A., 2009. Reaction induced fracturing during replacement processes. Contrib. Mineral. Petrol. 157, 127–133.
Kawano, S., Katayama, I., Okazaki, K., 2011. Permeability anisotropy of serpentinite and fluid pathways in a subduction zone. Geology 39 (10), 939–942.
Keppler, R., 2018. Crystallographic preferred orientations in eclogites–A review. Journal of Structural Geology 115, 284–296.
Korzhinskii, D.S., 1959. Physicochemical basis of the analysis of the paragenesis of minerals (Fiziko–khimicheskie osnovy analiza paragenezisov mineralov). Consultants Bureau, New York.
Locatelli, M., Verlaguet, A., Agard, P., Federico, L., Angiboust, S., 2018. Intermediate-depth brecciation along the subduction plate interface (Monviso eclogite, W. Alps). Lithos 320, 378–402.
Locatelli, M., Verlaguet, A., Agard, P., Pettke, T., Federico, L., 2019. Fluid pulses during stepwise brecciation at intermediate subductiondepths (Monviso eclogites, W. Alps): first internally then externally sourced. Geochem. Geophys. Geosyst. 20 (11), 5285–5318.
Lombardo, B., Nervo, R., Compagnoni, R., Messiga, B., Kienast, J.R., Mevel, C., Fiora, L., Piccardo, G.B., Lanza, R., 1978. Osservazioni preliminari sulle ofioliti metamorfiche del Monviso (Alpi Occidentali). Rend. Soc. It. Miner. Petrol. 34, 253–305.
Lombardo, B., Rubatto, D., Castelli, D., 2002. Ion microprobe U-Pb dating of zircon from a Monviso metaplagiogranite: implications for the evolution of the Piedmont-Liguria Tethys in the Western Alps. Ofioliti 27 (2), 109–117.
McNamara, D.D., Wheeler, J., Pearce, M., Prior, D.J., 2024. A key role for diffusion creep in eclogites: Omphacite deformation in the Zermatt-Saas unit, Italian Alps. J. Struct. Geol. 179, 105033.
Miller, D.P., Marschall, H.R., Schumacher, J.C., 2009. Metasomatic formation and petrology of blueschist-facies hybrid rocks from Syros (Greece): Implications for reactions at the slab–mantle interface. Lithos 107 (1), 53–67.
Morimoto, N., 1989. Nomenclature of pyroxenes. Mineralogical Journal 14 (5), 198–221.
Müller, W., Dallmeyer, R.D., Neubauer, F., Thöni, M., 1999. Deformation-induced resetting of Rb/Sr and 40Ar/39Ar mineral systems in a low-grade, polymetamorphic terrane (Eastern Alps, Austria). J. Geol. Soc. Lond. 156 (2), 261–278.
Muñoz-Montecinos, J., Behr, W.M., 2023. Transient Permeability of a Deep-Seated Subduction Interface Shear Zone. Geophys. Res. Lett. 50 (20).
Muñoz-Montecinos, J., Angiboust, S., Garcia-Casco, A., Glodny, J., Bebout, G., 2021. Episodic hydrofracturing and large-scale flushing 780 along deep subduction interfaces: Implications for fluid transfer and carbon recycling (Zagros Orogen, southeastern Iran). Chem. Geol. 781 (571), 120173.
Orzol, J., Stöckhert, B., Trepmann, C.A., Rummel, F., 2006. Experimental deformation of synthetic wet jadeite aggregates. J. Geophys. Res. Solid Earth 111 (B6).
Padrón-Navarta, J.A., Hermann, J., Garrido, C.J., López Sánchez-Vizcaíno, V., Gómez-Pugnaire, M.T., 2010. An experimental investigation of antigorite dehydration in natural silica-enriched serpentinite. Contributions to Mineralogy and Petrology 159, 25–42.
Peacock, S.M., 1990. Fluid processes in subduction zones. Science 248 (4953), 329–337.
Pétrequin, P., Sheridan, A., Cassen, S., Errera, M., Gauthier, E., Klassen, L., Rossy, M., 2011. Eclogite or jadeitite. Stone Axe Studies III, 55. Oxford: Oxbow Books. Davis, V., & Edmonds, M. R. (Eds.).

Philippot, P., van Roermund, H.L., 1992. Deformation processes in eclogitic rocks: evidence for the rheological delamination of the oceanic crust in deeper levels of subduction zones. J. Struct. Geol. 14 (8–9), 1059–1077.
Piepenbreier, D., Stöckhert, B., 2001. Plastic flow of omphacite in eclogites at temperatures below 500 C–implications for interplate coupling in subduction zones. Int. J. Earth Sci. 90 (1), 197–210.
Powell, R., Evans, K.A., Green, E.C., White, R.W., 2019. The truth and beauty of chemical potentials. J. Metamorph. Geol. 37 (7), 1007–1019.
Putnis, A., 2015. Transient porosity resulting from fluid–mineral interaction and its consequences. Rev. Mineral. Geochem. 80 (1), 1–23.
Putnis, A., Austrheim, H., 2010. Fluid-induced processes: metasomatism and metamorphism. Geofluids 10 (1–2), 254–269.
Reynard, B., 2013. Serpentine in active subduction zones. Lithos 178, 1–23.
Rubatto, D., Angiboust, S., 2015. Oxygen isotope record of oceanic and high-pressure metasomatism: a P–T–time–fluid path for the Monviso eclogites (Italy). Contrib. Mineral. Petrol. 170 (5), 1–16.
Rubatto, D., Hermann, J., 2001. Exhumation as fast as subduction? Geology 29 (1), 3–6.
Rubatto, D., Hermann, J., 2003. Zircon formation during fluid circulation in eclogites (Monviso, Western Alps): implications for Zr and Hf budget in subduction zones. Geochim. Cosmochim. Acta 67 (12), 2173–2187.
Rubatto, D., Williams, M., Markmann, T.A., Hermann, J., Lanari, P., 2023. Tracing fluid infiltration into oceanic crust up to ultra-high-pressure conditions. Contrib. Mineral. Petrol. 178 (11), 79.
Scambelluri, M., Fiebig, J., Malaspina, N., Müntener, O., Pettke, T., 2004. Serpentinite subduction: Implications for fluid processes and trace-element recycling. Int. Geol. Rev. 46 (7), 595–613.
Schwartz, S., Guillot, S., Reynard, B., Lafay, R., Debret, B., Nicollet, C., Lanari, P., Auzende, A.L., 2013. Pressure–temperature estimates of the lizardite/antigorite transition in high pressure serpentinites. Lithos 178, 197–210.
Shigeno, M., Mori, Y., Shimada, K., Nishiyama, T., 2012. Origin of omphacitites from the Nishisonogi metamorphic rocks, western Kyushu, Japan: comparison with jadeitites. Eur. J. Mineral. 24 (2), 247–262.
Skarbek, R.M., Rempel, A.W., 2016. Dehydration-induced porosity waves and episodic tremor and slip. Geochem. Geophys. Geosyst. 17 (2), 442–469.
Sorensen, S., Harlow, G.E., Rumble III, D., 2006. The origin of jadeitite-forming subduction-zone fluids: CL-guided SIMS oxygen-isotope and trace-element evidence. Am. Mineral. 91 (7), 979–996.
Spandler, C., Pettke, T., Rubatto, D., 2011. Internal and external fluid sources for eclogite-facies veins in the Monviso meta-ophiolite, western Alps: Implications for fluid flow in subduction zones. J. Petrol. 52 (6), 1207–1236.
Taetz, S., John, T., Bröcker, M., Spandler, C., Stracke, A., 2018. Fast intraslab fluid-flow events linked to pulses of high pore fluid pressure at the subducted plate interface. Earth Planet. Sci. Lett. 482, 33–43.
Tsujimori, T., 1997. Omphacite-diopside vein in an omphacitite block from the Osayama serpentinite melange, Sangun-Renge metamorphic belt, southwestern Japan. Mineralogical Magazine 61 (409), 845–852.
Tsujimori, T., Harlow, G.E., 2012. Petrogenetic relationships between jadeitite and associated high-pressure and low-temperature metamorphic rocks in worldwide jadeitite localities: a review. Eur. J. Mineral. 24 (2), 371–390.
Tursi, F., 2022. The key role of μ H2O gradients in deciphering microstructures and mineral assemblages of mylonites: examples from the Calabria polymetamorphic terrane. Mineralogy and Petrology 116 (1), 1–14.
Van Keken, P.E., Hacker, B.R., Syracuse, E.M., Abers, G.A., 2011. Subduction factory: Depth-dependent flux of H2O from subducting slabs worldwide. J. Geophys. Res. Solid Earth 116, B01410.
Vitale Brovarone, A., Alard, O., Beyssac, O., Martin, L., Picatto, M., 2014. Lawsonite metasomatism and trace element recycling in subduction zones. J. Metamorph. Geol. 32 (5), 489–514.
White, R.W., Powell, R., Holland, T.J.B., Johnson, T.E., Green, E., 2014. New mineral activity–composition relations for thermodynamic calculations in metapelitic systems. J. Metamorph. Geol. 32 (3), 261–286.
Whitney, D.L., Evans, B.W., 2010. Abbreviations for names of rock-forming minerals. Am. Mineral. 95 (1), 185–187.
Yui, T.F., Maki, K., Usuki, T., Lan, C.Y., Martens, U., Wu, C.M., Liou, J.G., 2010. Genesis of Guatemala jadeitite and related fluid characteristics: insight from zircon. Chem. Geol. 270 (1–4), 45–55.
Zertani, S., John, T., Brachmann, C., Vrijmoed, J.C., Plümper, O., 2022. Reactive fluid flow guided by grain-scale equilibrium reactions during eclogitization of dry crustal rocks. Contrib. Mineral. Petrol. 177 (6).
Zhang, J., Green II, H.W., Bozhilov, K.N., 2006. Rheology of omphacite at high temperature and pressure and significance of its lattice preferred orientations. Earth Planet. Sci. Lett. 246 (3–4), 432–443.